

# **Oh Boi Its my Thesis**

by

Anna Maria Houk

A thesis  
presented to the University of Waterloo  
in fulfillment of the  
thesis requirement for the degree of  
Masters of Science  
in  
Electrical and Computer Engineering - Quantum Information

Waterloo, Ontario, Canada, 2022

© 2022

### **Author's Declaration**

I hereby declare that I am the sole author of this thesis. This is a true copy of the thesis, including any required final revisions, as accepted by my examiners.

I understand that my thesis may be made electronically available to the public.

## **Abstract**

This is the abstract.

## Acknowledgements

## **Dedication**

# Table of Contents

<b>List of Figures</b>	viii
<b>List of Tables</b>	xi
<b>1 Introduction</b>	1
<b>2 Background</b>	2
2.1 Hollow-Core Photonic Crystal Fiber . . . . .	2
2.1.1 Conventional TIR Guidance . . . . .	2
2.1.2 Photonic Crystal Bandgap . . . . .	2
2.1.3 Bandgap Shift . . . . .	10
<b>3 Liquid-Filled HCPCF</b>	12
3.1 Filling Methods . . . . .	12
3.2 Experimental Set-Up . . . . .	14
3.3 H <sub>2</sub> O and D <sub>2</sub> O Transmission . . . . .	14
3.4 Results . . . . .	16
3.4.1 Selective Filling . . . . .	16
3.4.2 Full-Fiber Filling . . . . .	18
3.4.3 Particle-Mode Interaction and Optical Depth . . . . .	19
3.5 Indocyanine Green . . . . .	20
3.5.1 Experiment Set-Up . . . . .	26
3.5.2 ICG in HCPCF . . . . .	27

<b>4 Carbon Nanotubes</b>	<b>33</b>
4.1 Characterizing Carbon Nanotubes . . . . .	33
4.2 Nonlinear Optical Properties of CNTs . . . . .	38
4.3 Fluorescence of CNTs . . . . .	39
<b>5 Optical Excitation of Semiconductor Nanoparticles in Hollow-Core Fiber</b>	<b>42</b>
5.1 Bandgap Overlap . . . . .	42
5.1.1 Experiment Set-Up . . . . .	44
5.1.2 Expected Metrics . . . . .	46
<b>6 Conclusion</b>	<b>47</b>
6.0.1 Future Work . . . . .	48
<b>References</b>	<b>49</b>

# List of Figures

2.1	(a)cross-section of HCPCF highlighting the PC pattern (b)reduced to 1-dimension (2)in 2-dimensions . . . . .	3
2.2	Band plot for a 1D photonic crystal with parameters-, -, solved using Finite Difference Time Domain(FDTD) method[4]. . . . .	6
2.3	(a) primitive lattice vectors and (b) primitive reciprocal lattice vectors with first Brillouin zone (green) and irreducible Brillouin zone (red) depicted for a honeycomb lattice structure. . . . .	7
2.4	Band plot along the irreducible Brillouin zone for a honeycomb lattice with parameters -, -, . Solved for using Plane Wave Expansion(PWE) numerical method[4]. . . . .	9
3.1	Side profile of collapsed cladding 1550HC fiber running the fiber splicer with varying current strength and duration. . . . .	13
3.2	Variation between fibers using splicer settings 70ms 25ms . . . . .	13
3.3	Fiber transmission experimental set-up. . . . .	14
3.4	The transmission of heavy water(green) and regular water(blue) is shown for slabs of thickness ranging from 1cm to 8cm in increments of 1cm using absorption data recorded by [9]. . . . .	15
3.5	Transmission of H <sub>2</sub> O and D <sub>2</sub> O in (a)selectively-filled 800nm hollow-core fiber. . . . .	17
3.6	Modeshape of 1550 hollow-core fiber filled with (a)air (b)heavy water (c)distilled water. Fiber filled with heavy water maintains a Gaussian profile while the fiber with regular distilled water shows some distortion. . . . .	18
3.7	Transmission of H <sub>2</sub> O and D <sub>2</sub> O in fully-filled 1550nm hollow-core fiber. . . . .	18

3.8	(a) Depiction of the Homo-Lumo gap in organic semiconductors and the transition occurring between ground and excited states. (b) The chemical structure of ICG provided by MP Biomedicals. . . . .	20
3.9	Absorption cross-section at peak wavelengths 700nm(blue) and 780nm(green) for ICG dissolved in D <sub>2</sub> O(a) and H <sub>2</sub> O(b) . Data from (cite) was fitted using a linear regression model. . . . .	21
3.10	Degradation of a 4.5ppm initial concentration sample after 4hrs of light exposure reduced to a 2ppm concentration. . . . .	24
3.11	(a)Fluoresce spectrum of 4.5ppm sample (b) Maximum fluorescence and maximum absorption spectrum of 4.5ppm initial concentration sample . . .	25
3.12	(a) (b) . . . . .	26
3.13	Absorption spectrum of ICG samples (a) 2.5 ppm concentration in core of 800nm HCPCF and (b) 4 ppm concentration in core an d cladding of 1550nm HCPCF. . . . .	27
3.14	(a) The maximum fraction of fluorescence is plotted against excitation wavelength for a 4ppm ICG sample in a 1cm piece of 1550nm HCPCF and 1cm cuvette. The maximum fraction of fluorescence of the ICG in the cuvette is only 4% of that measured in fiber. (b) The optical density at each excitation wavelength. The fraction of fluorescence spectrum of the 4ppm ICG solution in (c) 1550nm HCPCF (d) a cuvette. . . . .	29
3.15	Measurements of 3.7ppm ICG sample in a 2cm piece of core-filled 800nm HCPCF (a) The maximum fraction of fluorescence and optical density against excitation wavelength. (b) The fraction of fluorescence spectrum (c) Measured output peak power and fractional fluorescence as a function of input power. . . . .	30
3.16	(a) (b) 2.28cm 0.44( $\frac{OD}{cm}$ ) 0.78cm 1.27( $\frac{OD}{cm}$ ) . . . . .	31
4.1	REPLACE Chiralities of CNTs with red dots indicating metallic and open dots [10]. . . . .	35
4.2	REPLACE Bands for (a)(c)Metallic and (b)(d)Semiconducting CNTs and their energy band gaps [12] . . . . .	35
4.3	Chiralities of CNTs with red dots indicating metallic and open dots Calculated gap energies between mirror-image spikes in density of states for $\gamma = 2.75$ eV. For (solid circles) metallic and (open circles) semiconducting, and (double circles) armchair CNTs. [15]. . . . .	37

4.4	Group characteristics of CNTs colored by (a)chiral angle and (b)diameter	41
5.1	Hollow-core fiber bandgap overlayed on CNT emission vs. excitation wavelengths	43
5.2	1550HC CNTs	43
5.3	(a) (b) fwhm=6nm (c)	44
5.4	(a) Absorbance spectrum of CNT sorted CNT sample (b)Absorbance of CNT sorted sample over 60 minutes, very low photobleaching.	45

# List of Tables

3.1	Absorption Cross Section parameter fitting of ICG dissolved in deionized water. Fitting done with linear regression on $\sigma$ vs. concentration data measured at $\lambda = 780nm$ from literature. . . . .	23
3.2	Absorption Cross Section parameter fitting of ICG dissolved in deionized water. Fitting done with linear regression on $\sigma$ vs. concentration data at $\lambda = 700nm$ from literature. . . . .	23
3.3	Absorption Cross Section parameter fitting of ICG dissolved in heavy water. Fitting done with linear regression on $\sigma$ vs. concentration data at $\lambda = 700nm$ from literature. . . . .	23
5.1	Thorlabs fiber bandgap shift. . . . .	42
5.2	CNTs with emission and excitation transmittable through HC1550 filled with D <sub>2</sub> O. . . . .	43

# **Chapter 1**

## **Introduction**

# Chapter 2

## Background

### 2.1 Hollow-Core Photonic Crystal Fiber

#### 2.1.1 Conventional TIR Guidance

#### 2.1.2 Photonic Crystal Bandgap

The 1D and 2D views of the structure

A periodic non-magnetic medium will have repeating dielectric constant [1]

$$\varepsilon(\mathbf{r}) = \varepsilon(\mathbf{r} + \mathbf{a}) \quad (2.1)$$

Due to its discrete and invariant translational symmetry, the dielectric constant along the medium can be expanded as the Fourier series

$$\varepsilon(\mathbf{r}) = \sum_{\mathbf{G}} \varepsilon_{\mathbf{G}} e^{i\mathbf{G}\cdot\mathbf{r}} \quad (2.2)$$

where  $\mathbf{G}$  are the reciprocal lattice vectors such that  $\mathbf{G} \cdot \mathbf{a} = 2\pi n$ . We can express the electric field also as the Fourier integral

$$\mathbf{E}(\mathbf{r}) = \iiint d^3\mathbf{k} \mathbf{A}(\mathbf{k}) e^{i\mathbf{k}\cdot\mathbf{r}} \quad (2.3)$$

Using the Maxwell equations (2.4) the wave equation can be written in terms of the electric field

$$\begin{cases} \vec{\nabla} \times \vec{H} &= -i\omega\epsilon(\vec{r})\vec{E} \\ \vec{\nabla} \times \vec{E} &= i\omega\mu_0\vec{H} \end{cases} \quad (2.4)$$

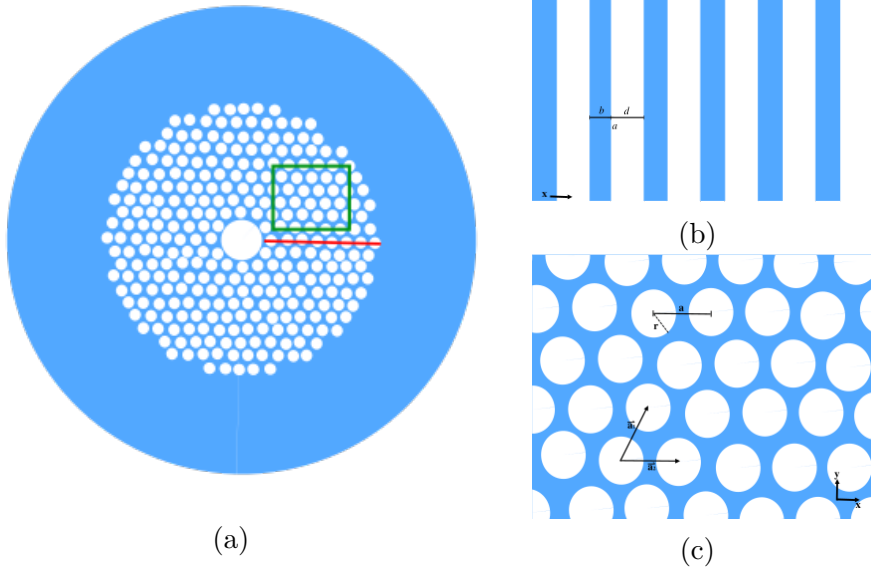


Figure 2.1: (a)cross-section of HCPCF highlighting the PC pattern (b)reduced to 1-dimension (2)in 2-dimensions

$$\nabla \times (\nabla \times \mathbf{E}) - \omega^2 \varepsilon(\mathbf{r}) \mu_0 \mathbf{E} = 0 \quad (2.5)$$

Substituting (2.2) and (2.3) into the above results in the dispersion relation:

$$\mathbf{k} \times (\mathbf{k} \times \mathbf{A}(\mathbf{k})) + \omega^2 \mu_0 \sum_{\mathbf{G}} \varepsilon_{\mathbf{G}} \mathbf{A}(\mathbf{k} - \mathbf{G}) = 0 \quad (2.6)$$

in where for any vector  $\mathbf{K}$  the solutions of (2.6) for the coefficient  $\mathbf{A}(\mathbf{K})$  are grouped with the coefficients  $\mathbf{A}(\mathbf{K} - \mathbf{G})$ , decoupling the coefficients of other vectors that cannot be expressed in the form  $\mathbf{K} - \mathbf{G}$ . Disregarding the decoupled vectors, the total electric field can be described as a superposition of normal modes with regard to a chosen vector  $\mathbf{K}$ :

$$\mathbf{E}_{\mathbf{k}}(\mathbf{r}) = \sum_{\mathbf{G}} \mathbf{A}(\mathbf{K} - \mathbf{G}) e^{i(\mathbf{k}-\mathbf{G}) \cdot \mathbf{r}} \quad (2.7)$$

we can pull out the Bloch theorem for the electric field from (2.7)

$$\mathbf{E}_{\mathbf{k}}(\mathbf{r} + \mathbf{a}) = e^{i\mathbf{k} \cdot \mathbf{a}} \mathbf{E}_{\mathbf{k}}(\mathbf{r}) \quad (2.8)$$

$$\mathbf{u}_{\mathbf{k}}(\mathbf{r}) = \sum_{\mathbf{G}} \varepsilon_{\mathbf{G}} e^{i\mathbf{G} \cdot \mathbf{r}} \quad (2.9)$$

$$\varepsilon_{\mathbf{G}} = \frac{1}{V} \int d^3 \mathbf{r} e^{-i\mathbf{G} \cdot \mathbf{r}} \mathbf{u}_{\mathbf{k}}(\mathbf{r}) \quad (2.10)$$

(Expand) Returning to (2.6), can fix  $\omega$  to find the corresponding  $\mathbf{K}$  and normal modes os the system. However, in the case of photonic crystals there are ranges of frequencies that have no  $\mathbf{K}$ s with real solutions, which implies that waves of these frequencies cannot propagate through the photonic crystal. These non-propagating frequencies are referred to as the photonic band gap.

## 1D Photonic Bandgap

Returning to the 1D periodic stack pictured in Fig. 2.1 the periodicity of dielectric constant is described by  $\varepsilon(z) = \varepsilon(z + p)$  where  $a = b + d$ , the length of one period. The reciprocal lattice vector will be  $\mathbf{G}_n = n \frac{2\pi}{a} \hat{z}$  and plugging into the Fourier series expansion of  $\varepsilon(z)$  from (2.2)

$$\varepsilon(z) = \sum_{n=-\infty}^{\infty} \varepsilon_n e^{in \frac{2\pi}{a} \hat{z}} \quad (2.11)$$

From the reduction to propagation in the z-direction with the electric field oriented in x-direction, (2.6) simplifies

$$K^2 A(K) + \omega^2 \mu_0 \sum_{n=-i\infty}^{\infty} \varepsilon_n A(K - n \frac{2\pi}{a}) = 0 \quad (2.12)$$

Expanding the Fourier coefficients to the 1st order and reducing the equations to the dominant coefficients of the form  $A(K)$  and  $A(K - \frac{2\pi}{a})$ .  $|K - g| = K$  and  $K = \frac{\pi}{a}$  gives a system of equations that can be solved to find the dispersion relation  $\omega(K)$ .

$$\begin{cases} (K^2 - \omega^2 \mu_0 \varepsilon_{00}) A(K) = \omega^2 \mu_0 \varepsilon_1 A(K - g) \\ \omega^2 \mu_0 \varepsilon_{-1} A(K) = ((K - g)^2 - \omega^2 \mu_0 \varepsilon_{00}) A(K - g) \end{cases} \quad (2.13)$$

The equations relating these two modes has a solution at

$$(K^2 - \omega^2 \mu_0 \varepsilon_{00}) ((K - g)^2 - \omega^2 \mu_0 \varepsilon_{00}) - (\omega^2 \mu_0 \varepsilon_1) (\omega^2 \mu_0 \varepsilon_{-1}) = 0 \quad (2.14)$$

noting  $\varepsilon_1 = \varepsilon_{-1}^*$  and  $K \approx 2g$  simplifies the relationship

$$\omega_{\pm}^2 = \frac{K^2}{\mu_0(\varepsilon_{00} \mp |\varepsilon_1|)} \quad (2.15)$$

The dispersion relation has two possible solutions, which specify the top and bottom of the photonic bandgap edges, as illustrated in Fig. 2.2.

If solving for the wavevector at a frequency between the two roots  $\omega_{\pm}$ , only complex solutions will exist. This means that only evanescent waves, not electromagnetic waves, propagate through the medium while the electromagnetic waves are reflected back; the medium acts as a mirror for the bandgap wavelengths.

This is the phenomenon that allows for HCPCF to guide certain frequencies of light: wavelengths in the bandgap are reflected by surrounding Bragg Grating confining them to the core of the fiber, while the rest are allowed to propagate through the grating.

## 2D Photonic Bandgap

To understand the full picture of light propagation in hollow-core fiber, we need to expand to the 2D case pictured in Fig. 2.1c. However, with the electromagnetic waves now propagating in two dimension there is an added layer of complexity with the TE TM wave polarizations and the bandgaps. In addition to controlling the refractive index of the

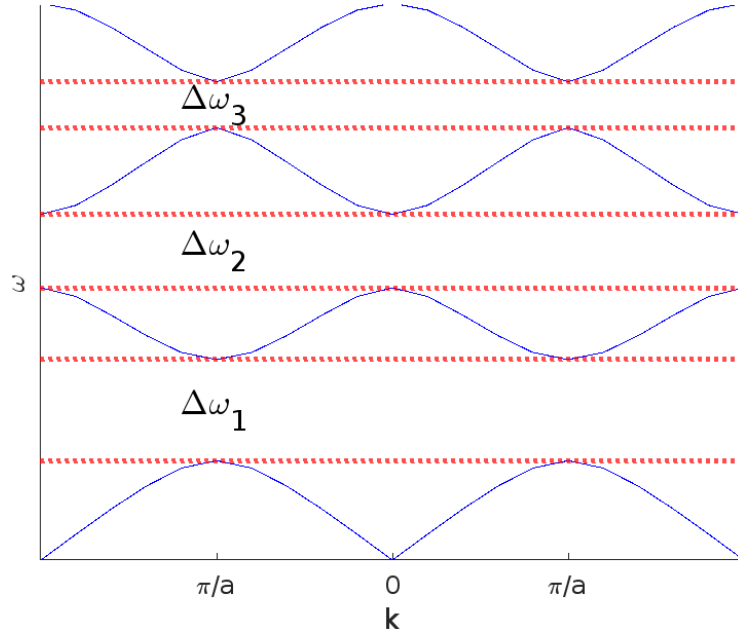
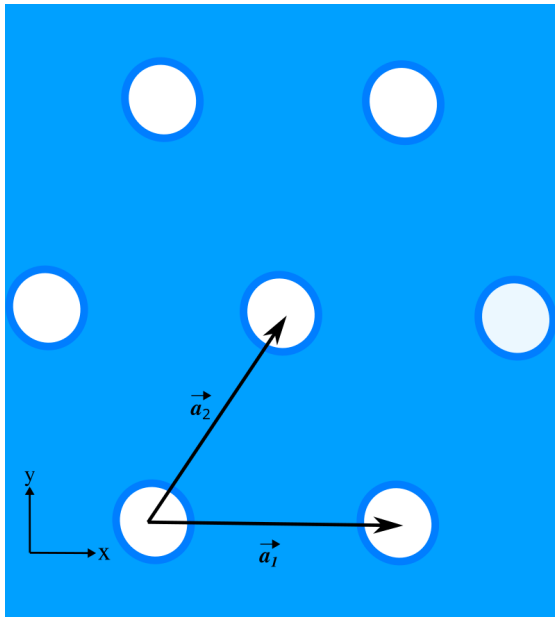
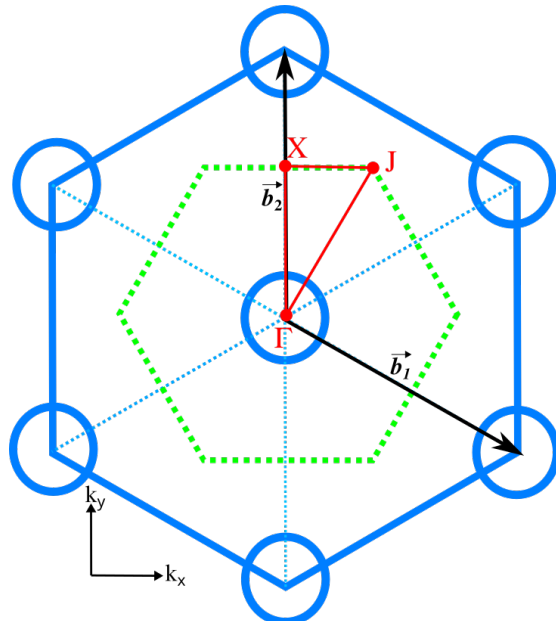


Figure 2.2: Band plot for a 1D photonic crystal with parameters-,-, solved using Finite Difference Time Domain(FDTD) method[4].

material and the period of the lattice, the lattice structure and hole radius will affect the performance of the photonic crystal, the latter playing a large role in the completeness of the photonic bandgap. In the 2D photonic crystal, the in-plane guided modes will have either magnetic fields in-plane and electric fields perpendicular to the lattice (TE modes), or electric fields in-plane and magnetic fields perpendicular to the lattice (TM modes). As the TE and TM modes are perpendicular to each other they may exhibit wildly different dispersion relations, which means that an optical bandgap is not guaranteed to persist for all polarizations[2]. This is certainly the case for square lattice phonic crystals, but other patterns such as the honeycomb (which is the structure in our HCPCF) do have a bandgap persisting for all polarizations[3]. This all to say, it is important to consider all polarization effects when making decisions about photonic crystal patterns for two or more dimensions.



(a)



(b)

Figure 2.3: (a) primitive lattice vectors and (b) primitive reciprocal lattice vectors with first Brillouin zone (green) and irreducible Brillouin zone (red) depicted for a honeycomb lattice structure.

Considering the lattice structure in Fig. 2.3(a), and taking propagation in the xy-plane ( $K_z = 0$  and  $z = 0$  for simplicity), the wavevector and position vectors reduce to  $\mathbf{K}_{||} = k_x \hat{x} + k_y \hat{y}$  and  $\mathbf{r}_{||} = x \hat{x} + y \hat{y}$ . The primitive lattice vectors of a honeycomb photonic crystal will be:

$$\mathbf{a}_1 = a \hat{x} \quad \mathbf{a}_2 = \frac{a}{2} \hat{x} + \frac{a\sqrt{3}}{2} \hat{y} \quad (2.16)$$

and transforming to the momentum-space,  $\mathbf{b} \cdot \mathbf{a} = 2\pi\delta_{ij}$ , as shown in Fig. 2.3(b) the primitive reciprocal lattice vectors are

$$\mathbf{b}_1 = \frac{2\pi}{a} \hat{x} - \frac{2\pi}{a\sqrt{3}} \hat{y} \quad \mathbf{b}_2 = \frac{4\pi}{a\sqrt{3}} \hat{y} \quad (2.17)$$

Taking these in combination of  $n, m$  integer scaling factors, the reciprocal lattice vector is defined  $\mathbf{G}_{||} = n\mathbf{b}_1 + m\mathbf{b}_2$ . The electromagnetic field defined for a two dimensional system

$$\mathbf{E}(\mathbf{r}) = e^{i\mathbf{k} \cdot \mathbf{r}} \sum_{m=-\infty}^{\infty} \sum_{n=-\infty}^{\infty} \mathbf{E}_{m,n} e^{i(n\mathbf{b}_1 + m\mathbf{b}_2) \cdot \mathbf{r}} \quad (2.18)$$

and the correlating Fourier expansion of dielectric function (2.10)

$$\varepsilon_{\mathbf{G}_{||}} = \frac{1}{a' \cdot b'} \int dx dy e^{i(G_x x + G_y y)} \mathbf{u}_k(x, y) \quad (2.19)$$

are substituted into (2.4). Utilizing the lattice symmetry and periodicity, the problem can be restricted to only solve for Bloch modes inside the of the irreducible Brillouin zone. The first Brillouin zone is defined by the perpendicular bisectors to the primitive reciprocal lattice vectors, depicted in green in Fig. 2.3(b) and can be further subdivided into the irreducible Brillouin zone shown in red. In order to find the photonic bandgap, solving the dispersion equation just along the irreducible Brillouin zone is sufficient. For a honeycomb lattice, the  $k$ -path to follow would be

$$\begin{cases} |\Gamma X| = \frac{2\pi}{a\sqrt{3}}, & k_x = 0, 0 < k_y < \frac{2\pi}{\sqrt{3}a} \\ |X J| = \frac{2\pi}{3a}, & 0 < k_x < \frac{2\pi}{3a}, k_y = \frac{2\pi}{\sqrt{3}a} \\ |\Gamma J| = \frac{4\pi}{3a}, & 0 < k_x < \frac{2\pi}{3a}, k_y = \sqrt{3}k_x \end{cases} \quad (2.20)$$

Discretizing (2.18) and (2.19) then picking a few points along the  $k$ -path, numerical methods can be used to solve for the optical bandgap. Fig. 2.4 shows the resulting TE bandgap for a honeycomb lattice with parameters-, using Plane Wave Expansion(PWE)[4].

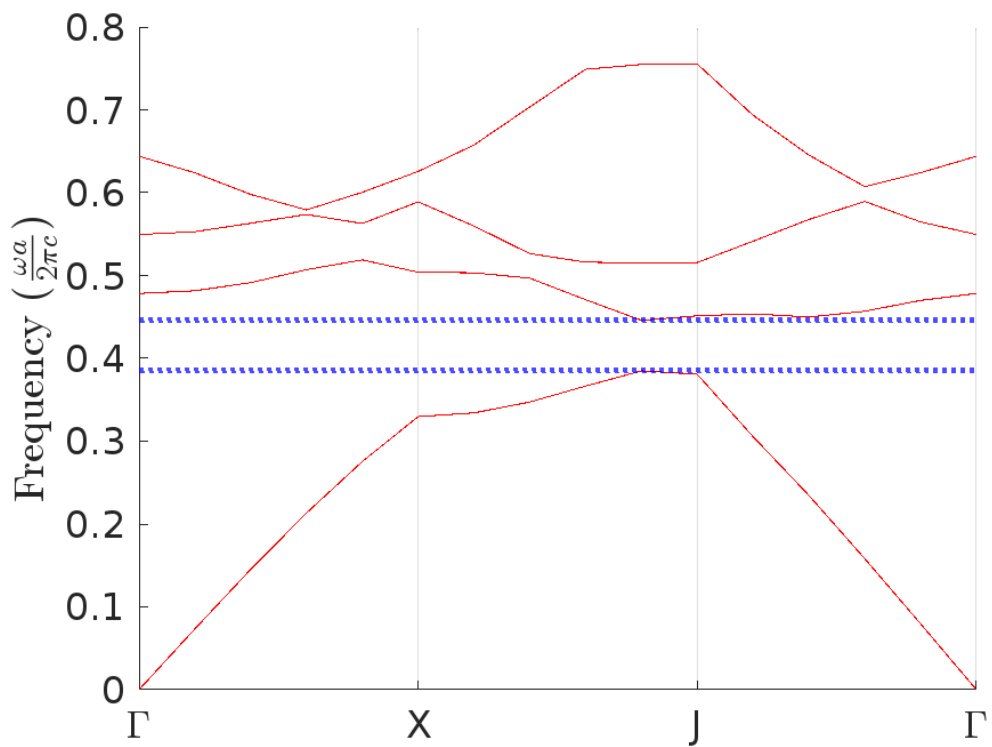


Figure 2.4: Band plot along the irreducible Brillouin zone for a honeycomb lattice with parameters  $-,-,$ . Solved for using Plane Wave Expansion(PWE) numerical method[4].

### 2.1.3 Bandgap Shift

The modal magnetic field distributions satisfy:

$$(\nabla_t^2 + k^2 n(\mathbf{r})^2 - \beta) \mathbf{H}(\mathbf{r}) = (\nabla_t \times \mathbf{H}(\mathbf{r})) \times (\nabla_t \ln(n(\mathbf{r})^2)) \quad (2.21)$$

This equation gives a scaling law for absolute refractive index at fixed contrast: “a solution for a transverse scale represented by  $\Lambda$  is replicated in an identical structure with a different  $\Lambda$  if the wavelength is scaled proportionately, to keep  $k\Lambda$  constant”

“We emphasise that the scalar wave equation (and therefore the scaling laws derived from it) is accurate for the smallest index contrasts only. However, for step-index structures the vector term in Eq. (2) only exists at boundaries, so the scalar wave equation accurately represents wave propagation elsewhere. Since bandgaps arise from interference and resonance effects among such generic waves, the scaling laws of Eq. (5) should be at least approximately valid” 1.45 RI contrast[5]

Scaling law for the wave equation for the transverse coordinates  $X = x\Lambda^{-1}$   $Y = y\Lambda^{-1}$  where  $\Lambda$  is a solution to the transverse scale.

$$n(X, Y) = \begin{cases} 1, & n_1 \text{ (high RI)} \\ 0, & n_2 \text{ (low RI)} \end{cases} \quad (2.22)$$

normalized scaled wave equation:

$$\nabla_{\perp}^2 \Psi + (v^2 n(X, Y) - w^2) \Psi = 0 \quad (2.23)$$

With  $\nabla_{\perp} = \partial^2 / \partial X^2 + \partial^2 / \partial Y^2$  solving for the frequency parameter  $v^2$  and eigenvalue  $w^2$ :

$$\begin{aligned} v^2 &= \Lambda^2 k^2 (n_1^2 - n_2^2) \\ w^2 &= \Lambda^2 (\beta^2 - k^2 n_2^2) \end{aligned} \quad (2.24)$$

from the equation above we see that the  $w^2$  is determined by the frequency parameter  $v^2$  and the index distribution function  $n(X, Y)$ . This implies that  $w^2$  and  $v^2$  are invariant with changes to the parameters  $k, \Lambda, n_1, n_2$ .  $k = \omega/c$   $\beta = k \cos \theta$  longitudinal component of the wavevector. Because the light propagates along the fiber, much of its wavevector is taken up by the longitudinal component.

In the HCPCF case where the glass refractive index is held constant and the air in the fiber is replaced by a new material the equations can be rewritten with  $n_1 = n_{glass}$  and  $n_2 = n_{air} = 1$ :

$$\begin{aligned} v^2 - w^2 &= \Lambda^2 (k^2 n_{glass} - \beta^2) \\ v &= k \Lambda n_{glass} \sqrt{n_{air} - \frac{n_{air}}{n_{new}}} \end{aligned} \quad (2.25)$$

The initial index contrast  $N_0 = \frac{n_{air}}{n_{glass}}$  moves to  $N = \frac{n_{new}}{n_{glass}}$  with the change in RI  $n_{air} < n_{new} < n_{glass}$ . This leads to the new center bandgap to be governed by the equation:

$$\lambda = \lambda_0 \sqrt{\frac{1 - N^{-2}}{1 - N_0^{-2}}} \quad (2.26)$$

This has been experimentally confirmed to hold for HCPCF [6].

# Chapter 3

## Liquid-Filled HCPCF

Our main experimental setup is centered on HCPCF that are filled with liquids, and contain carbon nanotubes (CNT) suspended in solution. In this chapter we provide a background on different filling methods we evaluated, the experimental setup utilized, and the observed characteristics in terms of transmission and absorption.

### 3.1 Filling Methods

In our experiments we tested two different filling methods: full fiber filling, and selective filling. We used a similar setup for both, but some additional steps are needed to achieve selective filling. For all our experiments we utilized fibers that we cut to be between 6cm and 8cm in length. To ensure consistent coupling and positioning, light was coupled to the core of the fiber by connecting to a solid-core PM780HP fiber via a mechanical splicing chip [7]. We replaced the air in 1550nm HCPCF with deionized water and heavy water by utilizing capillary action. To selectively fill the core of 800nm HCPCF, the photonic crystal cladding was collapsed while leaving the hollow-core open and is similarly filled with liquid using capillary action. We collapsed the cladding by placing the HCPCF opposite of a solid-core fiber in a fusion splicer [8] and adjusting arc current duration and power to melt the cladding structure while remaining distanced enough to prevent fusion with the solid-core fiber.

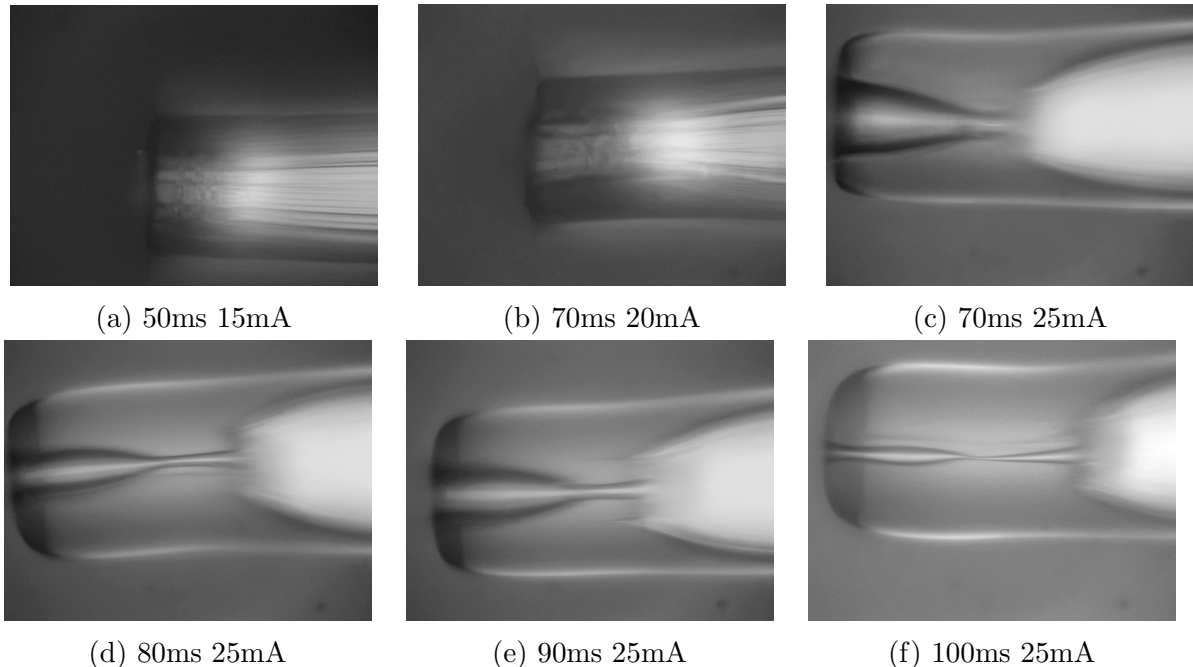


Figure 3.1: Side profile of collapsed cladding 1550HC fiber running the fiber splicer with varying current strength and duration.

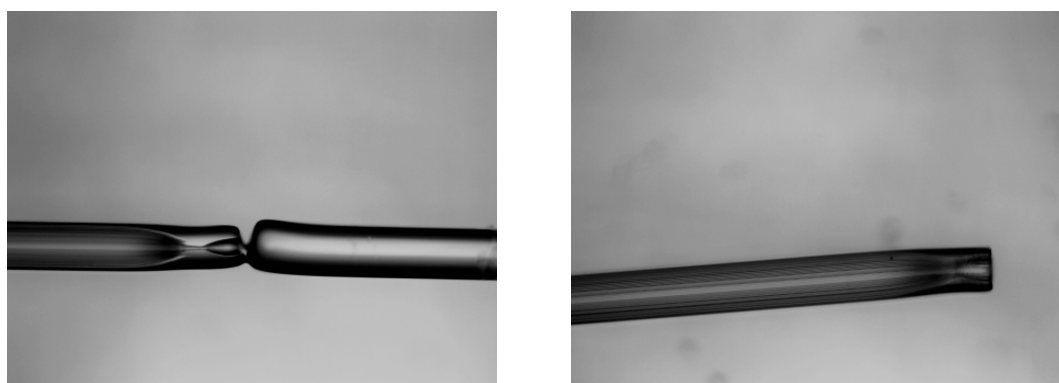


Figure 3.2: Variation between fibers using splicer settings 70ms 25ms

## 3.2 Experimental Set-Up

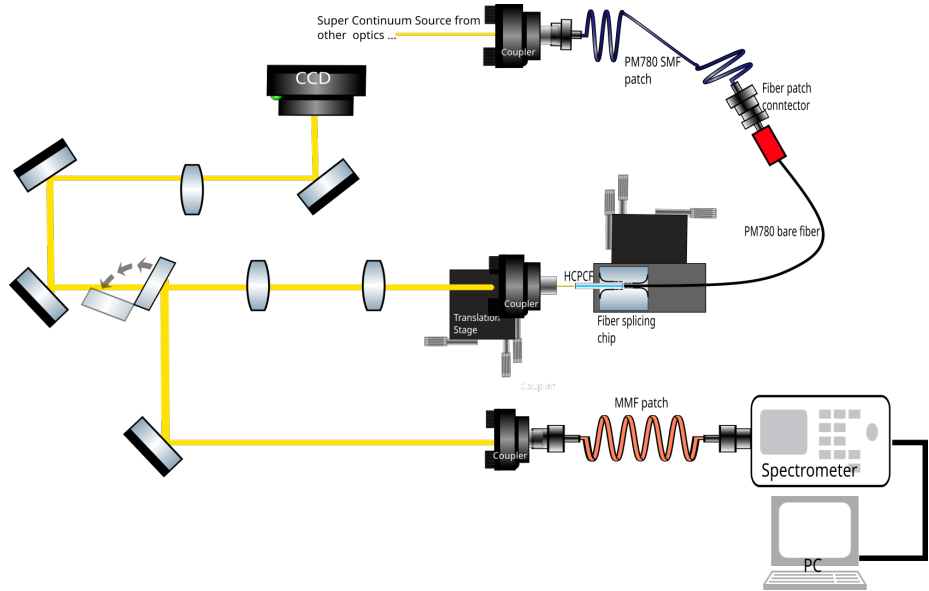


Figure 3.3: Fiber transmission experimental set-up.

## 3.3 $\text{H}_2\text{O}$ and $\text{D}_2\text{O}$ Transmission

HCPCF uses a photonic crystal cladding composed of a periodic silica structure that allows light to be guided through a hollow and thus low-refractive index core. In some applications of HCPCF, such as fiber-integrated sensors and on-linear optics, the hollow regions of the fiber are filled with liquids or gasses. Fibers that are fully-filled with water will produce a frequency shift in the bandgap due to refractive index scaling[6]. On the other hand, when the core is selectively filled with water, light will be guided via total-internal reflection. We investigate the transmission spectra of fully-filled and core-filled fibers for deionized water and heavy water.

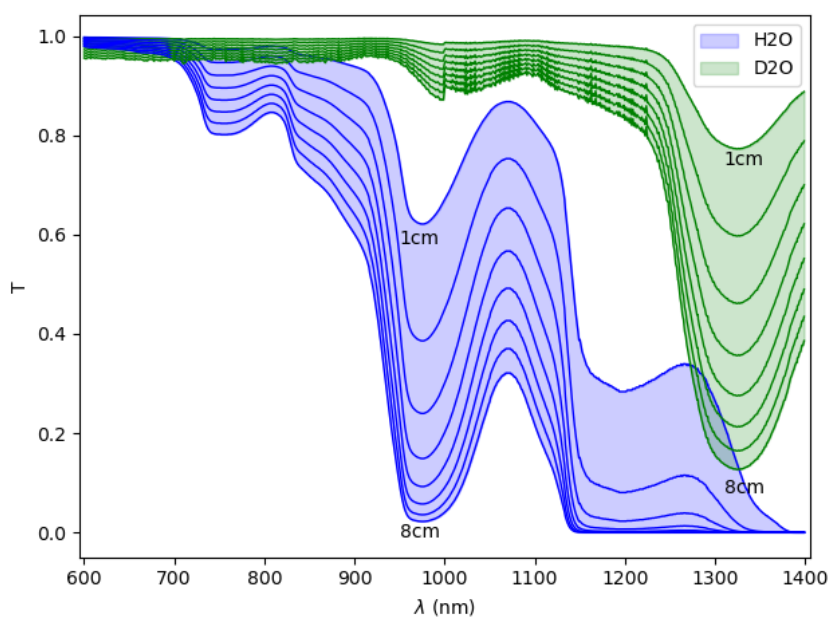


Figure 3.4: The transmission of heavy water(green) and regular water(blue) is shown for slabs of thickness ranging from 1cm to 8cm in increments of 1cm using absorption data recorded by [9].

## 3.4 Results

The air-filled 800nm HCPCF covers a transmission spectral range of 750nm–950nm. Light exits the fiber with a Gaussian mode shape and has an expected coupling between 75-80% when connected to a solid-core single-mode fiber. A water-filled core retains a Gaussian mode shape and has a 30% reduction in the normalized transmission for wavelengths above 850nm, which is consistent with the absorption spectrum of H<sub>2</sub>O [9]. We also observe that the coupling efficiency of the fiber drops to 31%. With a heavy water filled core, there are no significant changes in the normalized transmission spectrum, minimal effects to the absorption over this region, and coupling efficiency of up to 67%.

The air-filled 1550nm HCPCF covers a transmission spectral range of 1200nm–1700nm. With a filled core and cladding, the spectral range shifts to transmitting wavelengths between 600nm–1100nm for both heavy water and water, which aligns with the scaling laws prediction. Heavy water achieved a coupling efficiency of 47%, but water only 16%. The existing mode shape is roughly Gaussian but contains noise as some light also leaks from the photonic structure, worse for water than heavy water. The losses seen in water are not entirely explained, but losses and effects from the decrease in refractive index contrast are also present in the D<sub>2</sub>O-filled fiber. While there is a less than 20% difference in absorption coefficient between the 550nm–830nm for the fiber length, 7.6nm, between 830nm–950nm the absorption coefficient of water increases steeply but stays constant over the same region for heavy water.

### 3.4.1 Selective Filling

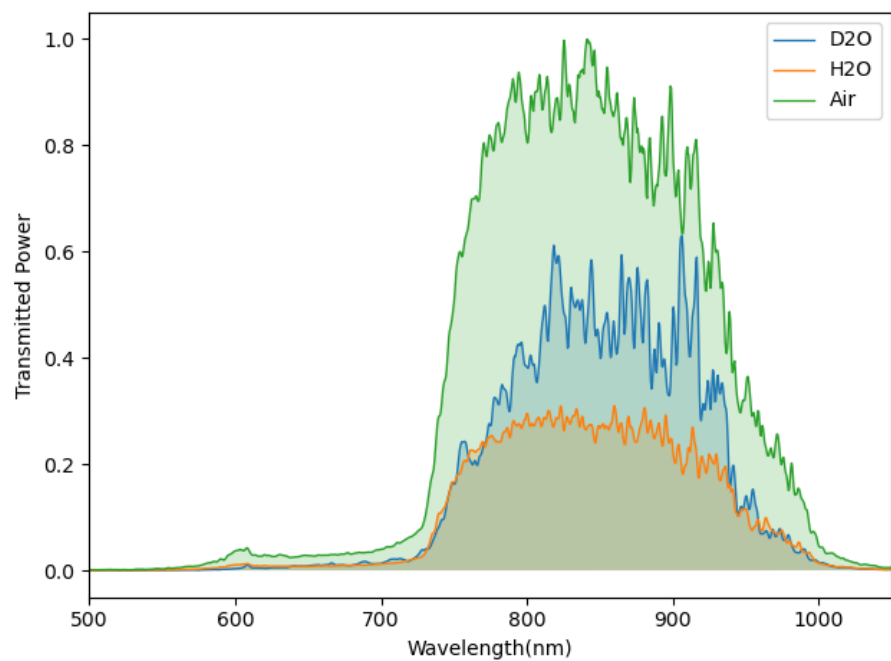


Figure 3.5: Transmission of H<sub>2</sub>O and D<sub>2</sub>O in (a)selectively-filled 800nm hollow-core fiber.

### 3.4.2 Full-Fiber Filling

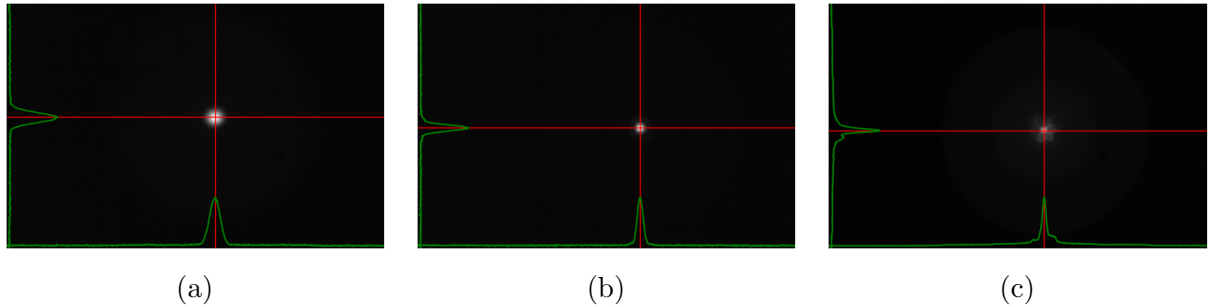


Figure 3.6: Modeshape of 1550 hollow-core fiber filled with (a)air (b)heavy water (c)distilled water. Fiber filled with heavy water maintains a Gaussian profile while the fiber with regular distilled water shows some distortion.

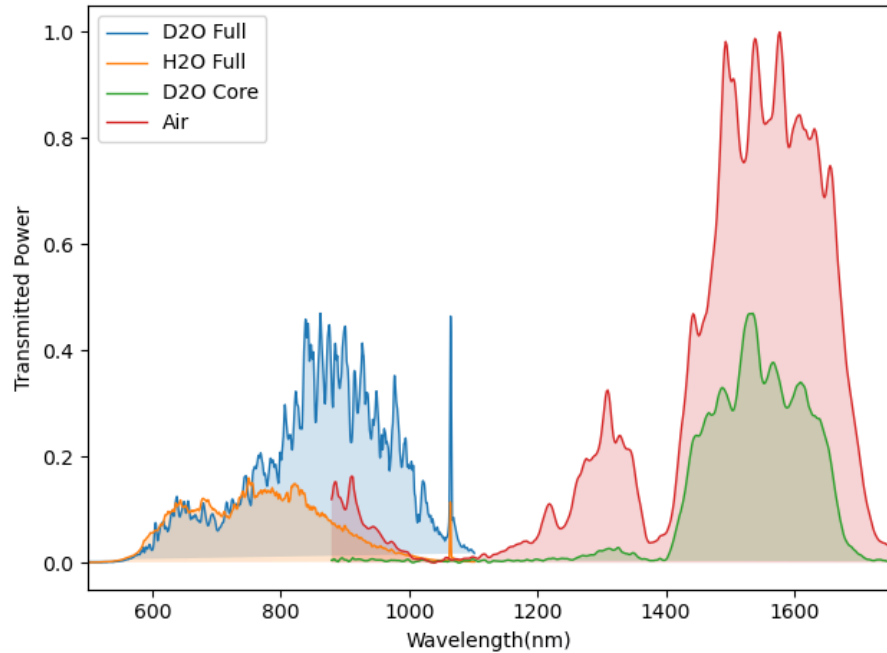


Figure 3.7: Transmission of  $\text{H}_2\text{O}$  and  $\text{D}_2\text{O}$  in fully-filled 1550nm hollow-core fiber.

### 3.4.3 Particle-Mode Interaction and Optical Depth

Optical depth (OD) is a measurement of the opacity of a system, related to the transmitted intensity by  $T = \exp(-OD)$ . With particles distributed throughout the fiber, the interaction between the beam and particles inside the fiber need to be taken into account. Similar considerations have been calculated for gas-filled HCPCF in cold-atom experiments [24, 25].

Beginning with a single particle interacting with the mode function of a waveguide, the strength of the particle interaction will depend on its position within the mode[26, 27]. The effective mode area of the waveguide is then relevant only in relation to the position of the particle.

$$\sigma_M = \frac{\int dx dy |f_k(x, y)|^2}{|f_k(x_p, y_p)|^2} \quad (3.1)$$

where  $f_k(x, y)$  is the transverse mode function and  $f(x_p, y_p)$  is the position of the particle. In the case of a Gaussian mode function (as would be in a HCPCF), the photon interaction with the particle will be stronger in the center of the mode and weak at the edges. The optical depth (OD) for a single particle the ratio of the scattering cross-section to that of the effective mode-area  $OD = \frac{\sigma_0}{\sigma_M}$ , so to find the optical depth over the entire ensemble the product of the number density of the sample and optical depth of each emitter is integrated over the volume :

$$OD_{fiber} = \int_0^{L'} \int_0^{r'} n(r, z) OD(2\pi r) dr dz \quad (3.2)$$

where  $r'$  and  $L'$  represent the radius and length of the ensemble. While the fibers are fully liquid cladding and core, due to the low interaction and guidance of photons in the PC structure an approximation is made constricting the mode function strictly to the core . This simplifies the dimensions of the integration to just be the radius and length of the fiber. This assumes that the particulates outside of the core do not have a significant contribution. If the distribution of molecules is take to be uniform along the fiber length and radius of the core, then the number density will be:

$$n(r, z) = \frac{N_{particle}}{V_{fiber}} = \frac{N_{particle}}{\pi r_{core}^2 L_{fiber}} \quad (3.3)$$

The integral will simplify to

$$\begin{aligned} OD_{fiber} &= \int_0^{L_{fiber}} \int_0^{r_{core}} n(r_{core}, L_{fiber}) \sigma_0 \frac{2}{\pi w_0^2} e^{-\frac{2r^2}{w_0^2}} (2\pi r) dr dz \\ &= N_{particle} \frac{\sigma_0}{\pi r_{core}^2} \left( 1 - e^{-\frac{2r_{core}^2}{w_0^2}} \right) \end{aligned} \quad (3.4)$$

### 3.5 Indocyanine Green

Due to the difficulty in isolating single-chirality solutions of CNTs, as outlined in the previous chapter, indocyanine green (ICG) - a fluorescent dye often used in microscopy imaging[35, 36] - was initially used in place of CNTs in the fiber. This particular dye is an organic semiconductor with Homo-Lumo gap calculations estimating a 2eV energy gap, with variations depending on the solvent[28]. The HOMO and LUMO energy levels in organic semiconductors are parallel to the maximum valence and minimum conduction, and the aforementioned energy gap falls within the range of energy bandgaps found in inorganic semiconductors.

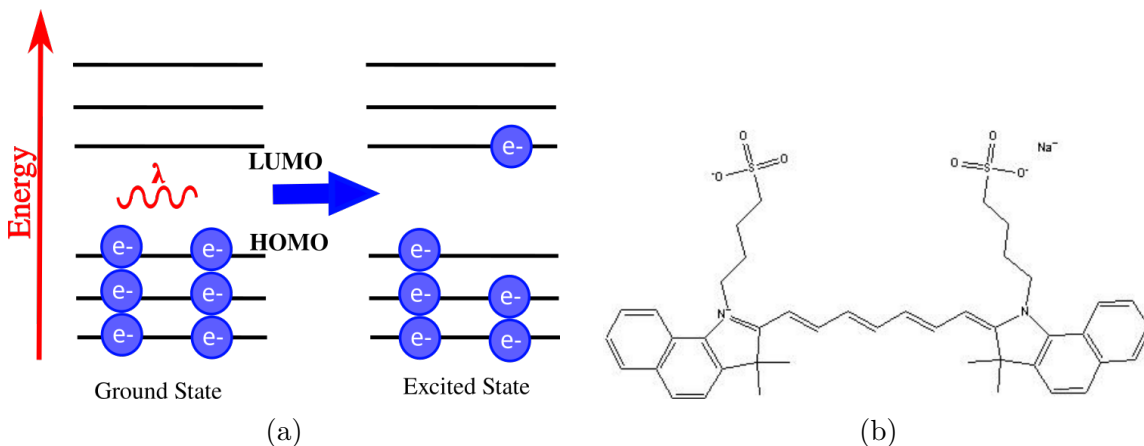


Figure 3.8: (a) Depiction of the Homo-Lumo gap in organic semiconductors and the transition occurring between ground and excited states. (b) The chemical structure of ICG provided by MP Biomedicals.

The following section details the the optical properties of ICG and measurements of the optical properties when confined in HCPCF.

### Absorption Cross-Section

ICG absorbs wavelengths between 600-900nm. The absorption is largely bimodal, with the greatest excitation occurring at 780nm and 700nm, but transforms into a monomeric distribution at 780nm at low concentrations and 700nm at high concentrations.

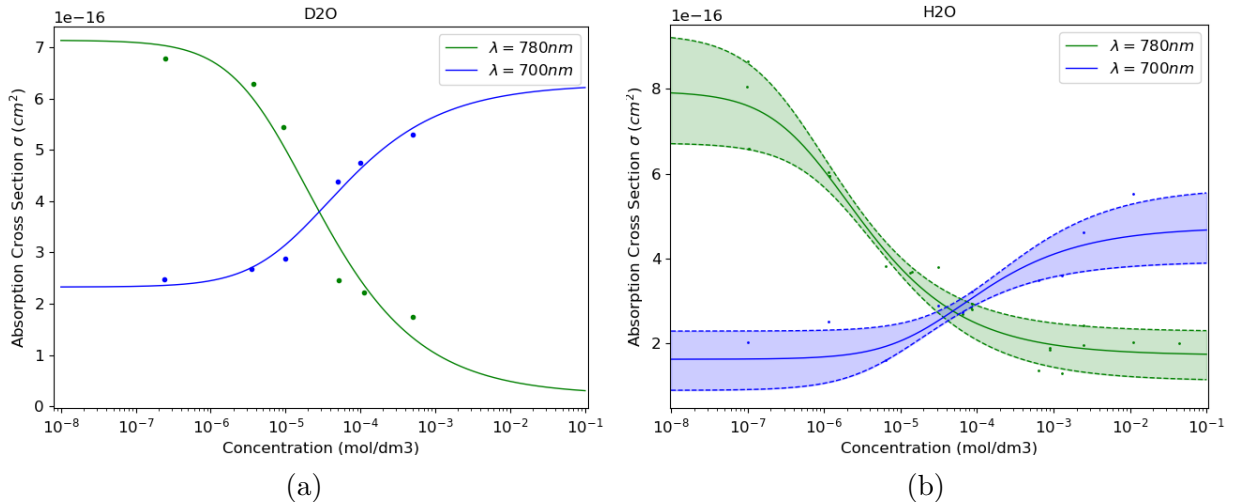


Figure 3.9: Absorption cross-section at peak wavelengths 700nm(blue) and 780nm(green) for ICG dissolved in D<sub>2</sub>O(a) and H<sub>2</sub>O(b) . Data from (cite) was fitted using a linear regression model.

Due to the chemical formation of ICG, the absorption of the molecule when dissolved in a solvent is highly concentration-dependent. ICG is made up of monomers, which are a type of molecule that can react with other monomers to form polymer chains. In the case of ICG, its monomers react with each other to form dimers, a chain of two join monomers. With higher concentrations monomers are closer to each other, causing the molecules to have an increased likelihood to shift from monomers to dimers, which in turn are less likely to be excited and shift the center absorption wavelength. The concentration of monomers  $M$  to dimers  $D$  is governed by the equilibrium reaction:



and law of mass action relation concentration

$$[D] = K_D[M]^2 \quad (3.6)$$

Where  $K_D$  is the dimerization constant . Written in terms of concentration  $C$  and mole fractions,  $[M] = x_M C = (1 - x_D)C$  and  $[D] = \frac{x_D}{2}C$ , the mole fraction of dimmers can be written in terms of the dimerization constant and concentration.

$$x_D = 1 + \frac{1}{4K_D C} - \sqrt{\left(1 + \frac{1}{4K_D C}\right)^2 - 1} \quad (3.7)$$

The absorption cross-section model for ICG[31, 33] will be an average of the effects of the of monomers and dimmers, where  $\sigma_M$  and  $\sigma_D$  are the monomer and dimer absorption cross-sections respectively.

$$\sigma = x_M \sigma_M + x_D \sigma_D = \sigma_M - x_D (\sigma_M - \sigma_D) \quad (3.8)$$

Plugging (3.7) into (3.8), remaining parameters could be found by doing a linear regression fit to absorption cross-section vs. concentration data from literature and the expected absorption cross-section could be calculated for any concentration. For ICG dissolved in H<sub>2</sub>O, the existing literature has some variation and so the upper/lower bounds and average were taken, while little data was available for ICG dissolved in D<sub>2</sub>O. The behavior in H<sub>2</sub>O and D<sub>2</sub>O are quite similar and are plotted in Fig. 3.9. At lower concentrations the absorption cross-section is slightly greater for D<sub>2</sub>O than H<sub>2</sub>O, with the reverse for high concentrations.

$\lambda_{peak} = 780nm$	$K_D$	$\sigma_M$	$\sigma_D$
[29]	$6.01 \times 10^5$	$9.29 \times 10^{-16}$	$2.28 \times 10^{-16}$
[30]	$1.03 \times 10^5$	$6.74 \times 10^{-16}$	$1.54 \times 10^{-16}$
[31]	$1.40 \times 10^5$	$6.72 \times 10^{-16}$	$1.11 \times 10^{-16}$
Average	$3.06 \times 10^6$	$7.94 \times 10^{-16}$	$1.72 \times 10^{-16}$

Table 3.1: Absorption Cross Section parameter fitting of ICG dissolved in deionized water. Fitting done with linear regression on  $\sigma$  vs. concentration data measured at  $\lambda = 780nm$  from literature.

$\lambda_{peak} = 700nm$	$K_D$	$\sigma_M$	$\sigma_D$
[29]	$3.00 \times 10^3$	$2.29 \times 10^{-16}$	$25.68 \times 10^{-16}$
[31]	$3.06 \times 10^4$	$8.89 \times 10^{-16}$	$3.93 \times 10^{-16}$
Average	$9.31 \times 10^3$	$1.62 \times 10^{-16}$	$4.74 \times 10^{-16}$

Table 3.2: Absorption Cross Section parameter fitting of ICG dissolved in deionized water. Fitting done with linear regression on  $\sigma$  vs. concentration data at  $\lambda = 700nm$  from literature.

$\lambda_{peak}$	$K_D$	$\sigma_M$	$\sigma_D$
780nm	$3.22 \times 10^4$	$7.14 \times 10^{-16}$	$2.68 \times 10^{-17}$
700nm	$1.67 \times 10^4$	$2.833 \times 10^{-16}$	$6.28 \times 10^{-16}$

Table 3.3: Absorption Cross Section parameter fitting of ICG dissolved in heavy water. Fitting done with linear regression on  $\sigma$  vs. concentration data at  $\lambda = 700nm$  from literature.

## Photostability

At high concentrations, ICG behaves as a “J-aggregate”, a category of dyes that shift in the absorption band to larger wavelengths in certain solvents. When mixed into water and other solvents, ICG shifts over time to a center wavelength of 893nm. This process can be accelerated under high heat. In high-concentration forms (in the range of 1000ppm solutions) [32], J-aggregates can be stored at room temperature for several months. However, in such a state the dye will be too optically dense to observe any optical excitation and when diluted to perform such measurements, the J-aggregates will begin to detach into smaller molecules within 24hrs. The effects of dye concentration of storage life in aqueous solutions becomes a tricky balance at single-digit ppm concentrations. At that concentration, the fluorescence intensity of the dye is at its greatest but it degrades to undetectable levels in just a couple of hours under optimal storage conditions[30, 34]. The rate of deterioration occurs linearly based on the initial concentration of ICG[29], but the amount of light exposure of the solution will also exasperate the degradation rate[34].

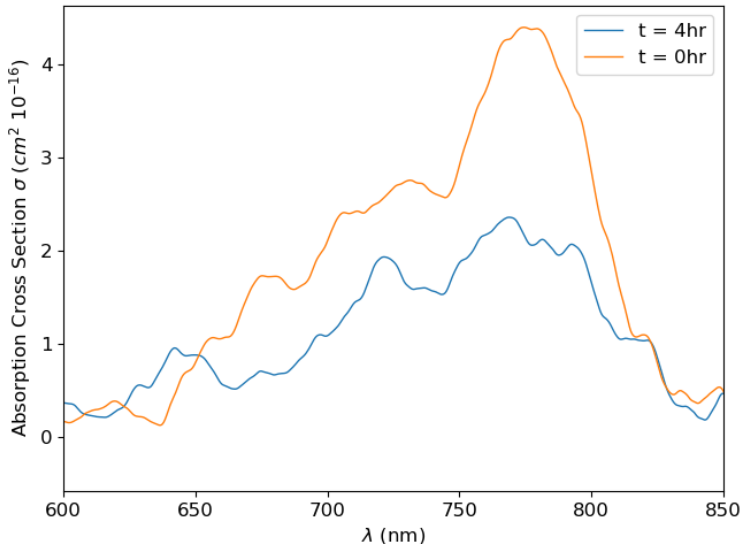


Figure 3.10: Degradation of a 4.5ppm initial concentration sample after 4hrs of light exposure reduced to a 2ppm concentration.

## Fluorescence

Photoluminescence in the dye is observed in the range of 750-900nm, therefore overlapping with the absorption spectrum. The peak emission wavelength for ICG varies within 800nm-820nm[33, 34] when excited at 780nm, and decreases as solution concentration increases, The dimerization effects are attributed to (a) The formation of weakly fluorescent ICG molecular aggregates at high concentrations (b) self-quenching and (c) re-absorption of the emitted fluorescence by the ICG molecules due to overlap of the absorption and emission spectra. In the J-aggregate form the excitation wavelength shifts to 834nm and the emission peaks at 890nm although low quantum yield and strong light scattering does not lend to accurate measurements[32].

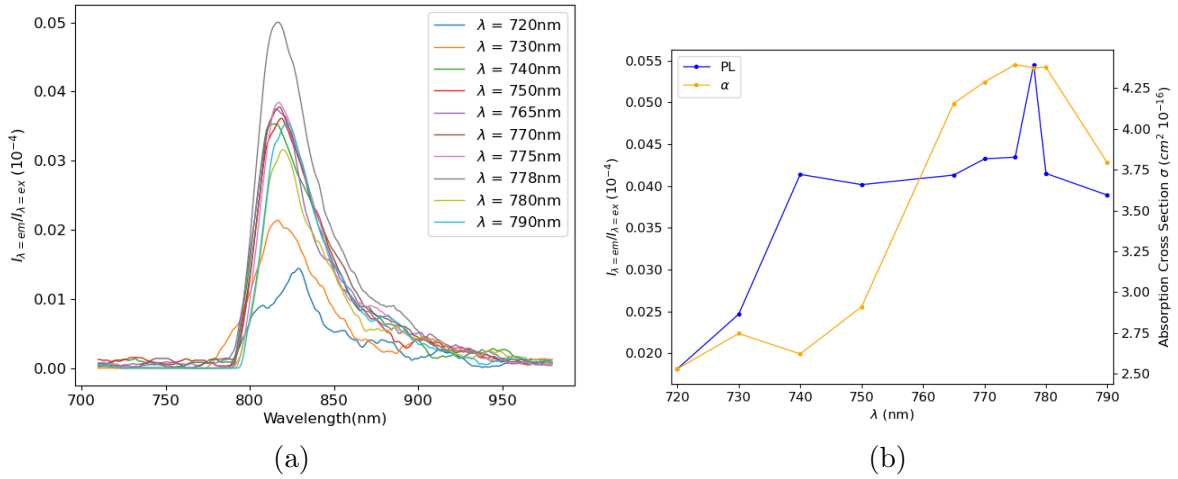


Figure 3.11: (a) Fluorescence spectrum of 4.5 ppm sample (b) Maximum fluorescence and maximum absorption spectrum of 4.5 ppm initial concentration sample

### 3.5.1 Experiment Set-Up

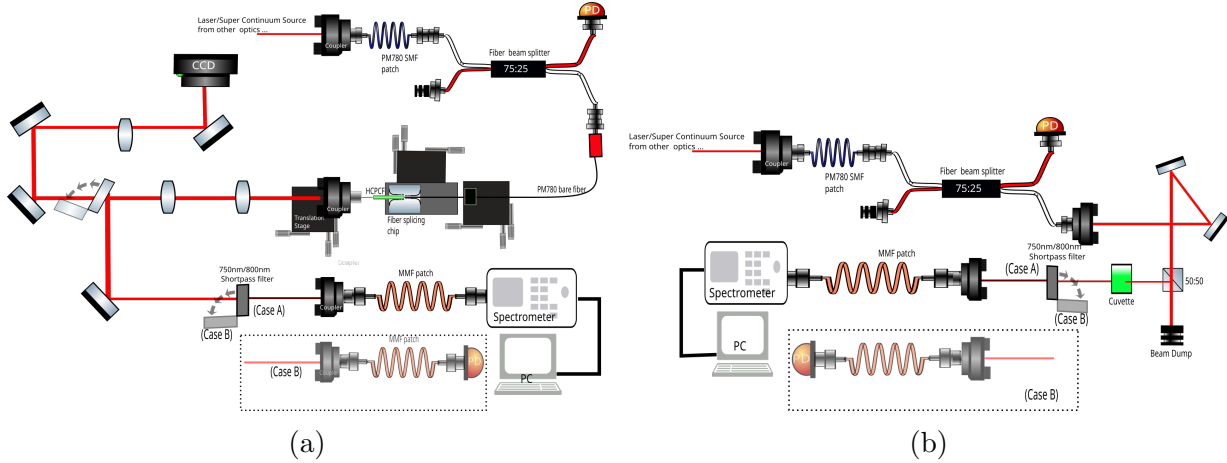


Figure 3.12: (a) (b)

Preparation

#### 1. Stock

- Using the micropipette, measure 1ml of D<sub>2</sub>O or H<sub>2</sub>O into a vial
- Using the scale, measure 1mg of ICG powder
- Pour the measured ICG into the 1ml of D<sub>2</sub>O/H<sub>2</sub>O
- Close the vial and shake for 15 seconds to dissolve

#### 2. Dilution

- Measure 5ml of D<sub>2</sub>O or H<sub>2</sub>O into a vial
- Using the pipette, measure 10ul of the stock solution
- Output the 10ul of stock solutions into the 100ml of D<sub>2</sub>O/H<sub>2</sub>O
- Close the vial and shake for 15 seconds to dissolve

Used within 12 hrs of creation

### 3.5.2 ICG in HCPCF

We prepared low-concentration samples of dye, and subsequently we used it to fill a 800nm HCPCF core and 1550nm HCPCF core and cladding. We measured the absorption spectrum of the dye, though muddled by additional losses from the fiber, as shown in Fig. 3.13. Additionally, there is an observed 18nm shift in the peak absorption from 778nm to 796nm in the 1550nm bandgap-shifted liquid-filled fiber, while the 800nm liquid-core fiber has an insignificant 4nm shift in peak from 775nm to 771nm.

For 800nm core-filled HCPCF, ICG solutions were prepared with  $H_2O$  and  $D_2O$  sol-

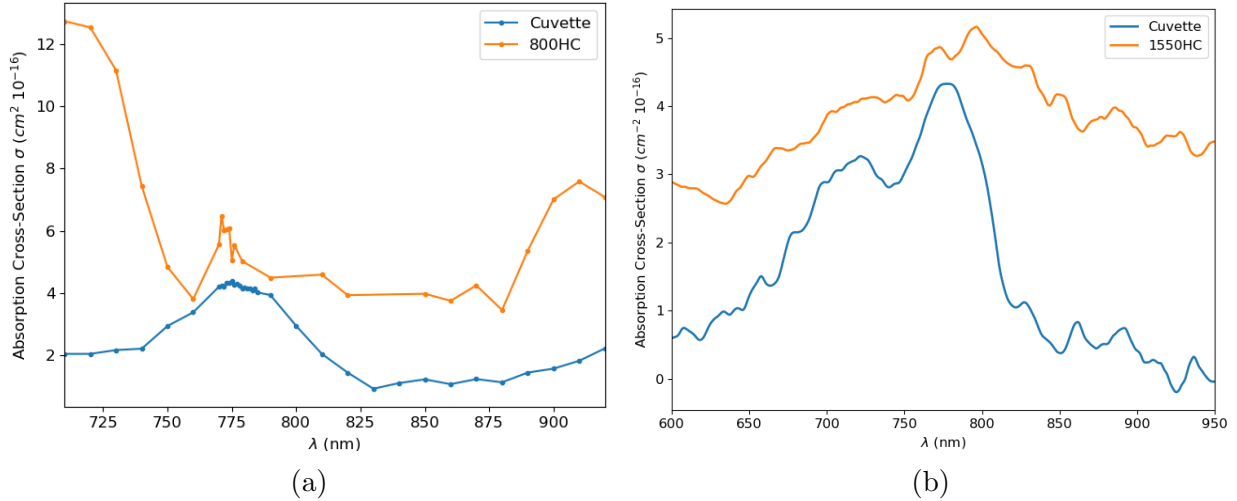


Figure 3.13: Absorption spectrum of ICG samples (a) 2.5 ppm concentration in core of 800nm HCPCF and (b) 4 ppm concentration in core and cladding of 1550nm HCPCF.

vents, but fluorescence was only guided in the  $D_2O$ . In the 800HC fiber there was already significant loss coming from the narrow bandgap in combination with lower refractive index contrast of using a liquid medium, as half of the absorption spectrum is outside the bandgap; We suspect that the absorption of effects of  $H_2O$  in the NIR (discussed in chapter 2) and re-absorption from the overlapping excitation-emission spectra was greater than the number of emitted photons. The fluorescence guided in the 800nm HCPCF was also influenced by the bandgap, shown in Fig. 3.15b. The emission had a large shifts in peak for excitation between 745 – 775nm - wavelengths at the edge of the bandgap and with high absorption effects- varying peak fluorescence between 800 – 820nm while for excitation above 775nm the fluorescence stayed centered at 805nm.

We detected fluorescence also in ICG-filled 1550nm HCPCF with D<sub>2</sub>O as solvent, which had the best ratio of fluorescence intensity to emission intensity (“fraction of fluorescence”). For a 4ppm ICG sample the fraction of fluorescence are compared in Fig. 3.14 for excitation wavelengths below the emission wavelength range. The peak fluorescence in the cuvette was at 820nm, but was shifted down 10nm to 810nm in the fiber and the fraction of fluorescence in 1550nm HCPCF was  $\sim 35\times$  greater than that measured through the cuvette. For the 3.7ppm sample in 800nm HCPCF we measured similar fraction of fluorescence to the cuvette sample at the excitation wavelength of peak absorption(778nm), although the exact source of the large difference in fraction of fluorescence in the 1550nm and 800nm HCPCF/cuvette are not clear.

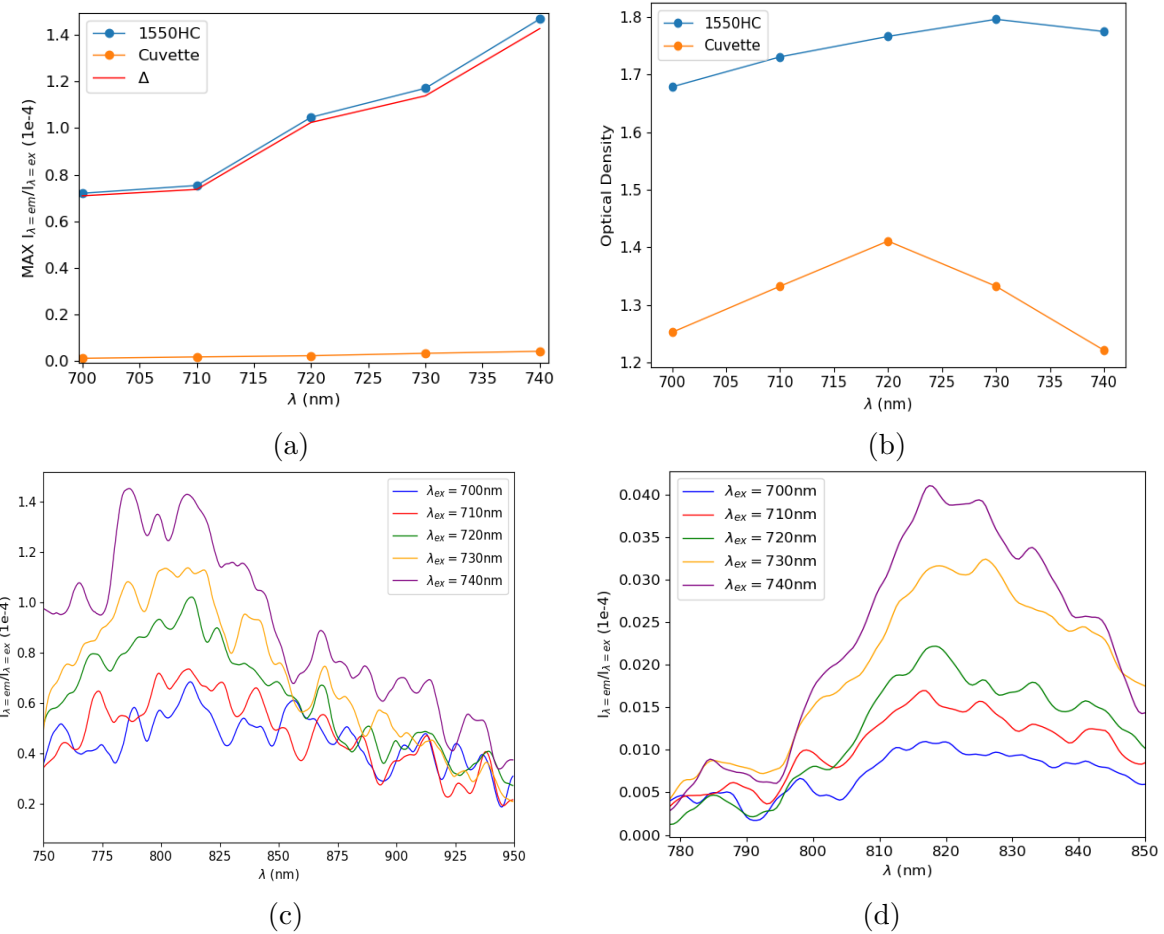


Figure 3.14: (a) The maximum fraction of fluorescence is plotted against excitation wavelength for a 4ppm ICG sample in a 1cm piece of 1550nm HCPCF and 1cm cuvette. The maximum fraction of fluorescence of the ICG in the cuvette is only 4% of that measured in fiber. (b) The optical density at each excitation wavelength. The fraction of fluorescence spectrum of the 4ppm ICG solution in (c) 1550nm HCPCF (d) a cuvette.

At the maximum absorption wavelength, the fraction of fluorescence and output power at the excitation wavelength are measured as a function of the input power, shown in Fig. 3.15c. The fraction of fluorescence peaks at an input power of  $50\mu W$  and slowly decreases linearly with a rate of – while the output power increases logarithmically and appears to approaching a limit on the transmission. Overall, the collection efficiency is of  $5.1 \times 10^{-4}\%$  in the 800nm HCPCF and based on its trend we expect the collection efficiency of the 1550nm HCPCF to not be much greater than the 0.014% measured at  $\lambda_{ex} = 740\text{nm}$ . In other words, for milliwatts of pump power we expect to get nanowatts at the emission frequency.

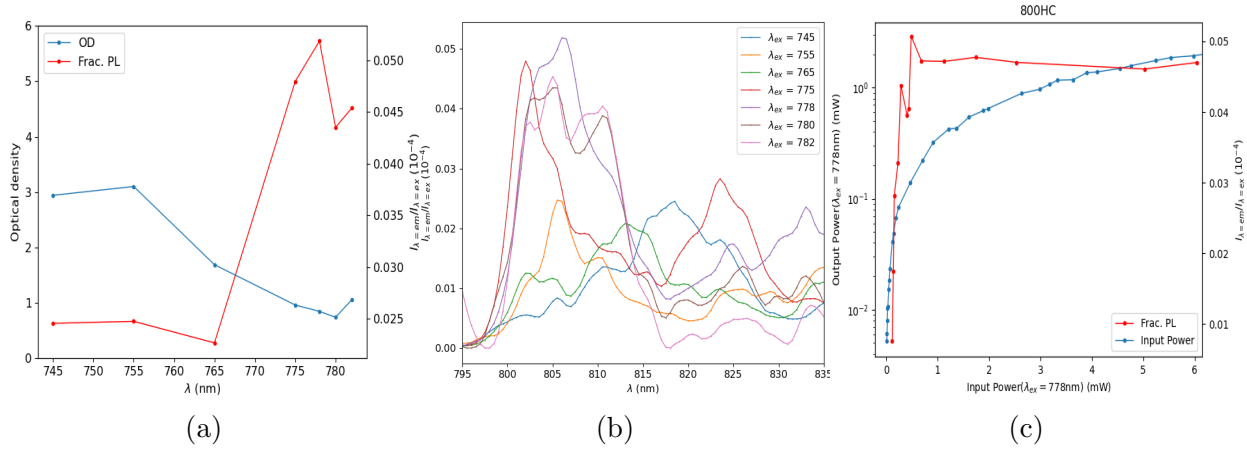


Figure 3.15: Measurements of 3.7ppm ICG sample in a 2cm piece of core-filled 800nm HCPCF (a) The maximum fraction of fluorescence and optical density against excitation wavelength. (b) The fraction of fluorescence spectrum (c) Measured output peak power and fractional fluorescence as a function of input power.

## Optical Density Calculations

For ICG dispersed in water, molecule aggregate radii have been measured between  $2\text{nm} - 200\text{nm}$  [37] with J-aggregates forming at radii  $> 50\text{nm}$  [38]. Due to the low concentration samples of dye used in our experiments, we expect the lower range of molecule diameter, meeting the Raleigh scattering approximation condition  $\frac{2\pi r}{\lambda} \ll 1$ , the scattering cross-section is

$$\sigma_0 = \frac{2\pi^5(2r_{particle})^6}{3\lambda^4} \left( \frac{N^2 - 1}{N^2 + 2} \right)^2 \quad (3.9)$$

where  $N = \frac{n_{particle}}{n_{solvent}}$ . Applying the parameters above and (3.9) to (3.4) the estimated concentration of ICG molecules for optically dense medium ( $OD_{fiber} = 1$ ) has a range of  $N_{particle} = 1.5 \times 10^8 \sim 2.0 \times 10^{14}$  molecules and  $N_{particle} = 8.2 \times 10^7 \sim 1.1 \times 10^{14}$  molecules for 1550nm and 800nm HCPCF respectively varying the ICG aggregate radii within the approximation condition.

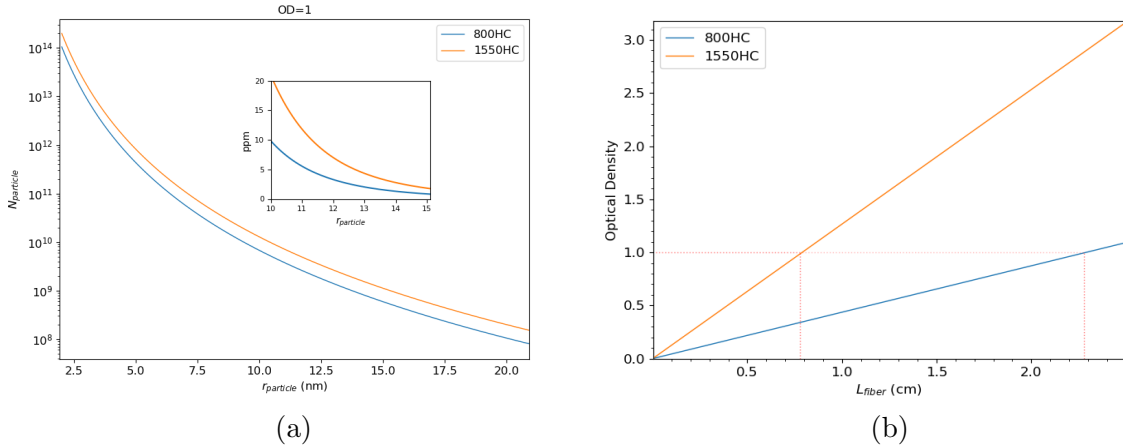


Figure 3.16: (a) (b)  $2.28\text{cm} \ 0.44(\frac{OD}{cm}) \ 0.78\text{cm} \ 1.27(\frac{OD}{cm})$

For calculations of optical density with ICG molecules in the 1550nm HCPCF, the core radius is taken as  $r_{core} = 5 \pm 0.05\mu\text{m}$  with beam waist  $w_0 = 4.5 \pm 0.05\mu\text{m}$ . For this  $L_{fiber} = 1\text{cm}$  piece of fiber, the number of molecules contained in a perfectly filled core is expected to be

$$N_{particle} = M_{ICG} * C * V_{fiber} = \frac{1\text{mol}}{774.98\text{g}} * \frac{4\text{mg}}{1\text{dm}^3} * \pi(5\mu\text{m})^2(1\text{cm}) = 2.441 \times 10^9 \text{molecules} \quad (3.10)$$

Using the measured optical density in the fiber, Fig. 3.14b the estimated radius of the aggregate ICG molecules is  $r_{particle} = 13.7 \pm 0.2\text{nm}$ . Carrying out the same calculations for the  $L_{fiber} = 2\text{cm}$  800nm HCPCF, the number of molecules contained in a perfectly filled core will be  $N_{particle} = 2.54 \times 10^9$ . The fiber has a core radius  $r_{core} = 3.75 \pm 0.05\mu\text{m}$  with beam waist  $w_0 = 2.75 \pm 0.05$  and using the measured optical density in the fiber, Fig. 3.15a, the estimated radius of the aggregate ICG molecules is  $r_{particle} = 11.5 \pm 0.26\text{nm}$ . These molecule radii are well in agreement, but since the 800nm HCPCF ICG solution is a slightly lower concentration the average  $r_{particle}$  is expected to form slightly smaller aggregates.

# Chapter 4

## Carbon Nanotubes

First discovered by S.Iijima and T. Ichihashi in 1993, carbon nanotubes (CNT) are single layers of graphene rolled up into a hollow cylinder near 1 nm in diameter and near 1um in length. While graphene is a 2-dimensional material, the dimensions of CNTs allow them to be treated as 1-dimensional materials. Carbon nanotubes possess extremely interesting optical properties that make them interesting to use, and they have the advantage of not degrading quickly, contrary to ICG. In this section we are going to describe the attributes that make them so attractive from an optical standpoint, characterizing them in relation to their chirality, nonlinear optical properties, and fluorescence.

### 4.1 Characterizing Carbon Nanotubes

The main descriptive properties of CNTs are the chiral vector, which is a scaled integer-valued combination of the unit vectors for the honeycomb structure of graphene, written in the form (n, m).

$$C_h = na_1 + ma_2 = (n, m) \quad (4.1)$$

The unit vectors in Cartesian coordinates are

$$a_1 = \left(\frac{\sqrt{3}}{2}, \frac{1}{2}\right)\sqrt{3}a_{C-C}a_2 = \left(\frac{\sqrt{3}}{2}, -\frac{1}{2}\right)\sqrt{3}a_{C-C} \quad (4.2)$$

and have equal length , where is the length of the carbon bond, which for graphene is 1.421 (Å) (where  $1\text{\AA} = 10^{-10}\text{m}$ ), and often approximated as 1.44(Å) for CNTs, though there is variation depending on the curvature of the nanotubes[13]. The chiral vector is of

high value as it reveals a lot of information about the electronic and optical properties of individual CNTs. The chiral angle  $\theta$ , the angle between the unit vectors, gives the direction of the chiral vector and is defined as

$$\theta = \tan^{-1} \left[ \frac{m\sqrt{3}}{m + 2n} \right] \quad (4.3)$$

and the diameter of a nanotube as

$$d_t = \frac{a_{CC}\sqrt{3}}{\pi} \sqrt{n^2 + nm + m^2} \quad (4.4)$$

Due to the geometry of graphene, CNTs have a six-fold rotational symmetry and the connection points of the lattice, i.e. the way that the graphene is rolled into a tube will produce equivalent CNTs between as , thus the tube geometries are often constrained to the first range. Nanotubes with a chiral angle of are called zigzag tubes and chiral angles of are called armchair tubes due to the pattern made by their circumference as shown in the Figure 2, and are the two configurations in which CNTs are anti chiral, meaning that their structures are indistinguishable from their mirrored image, while all in between-angled nanotubes are chiral, i.e. distinguishable from their mirrored image. The diameter and angle actually vary the electronic band structure of the CNT significantly. CNTs have an additional electron confinement around their circumference[12]and as can be seen from the above definitions, the tube diameter of CNTs is quantized and varies depending on how the graphene honeycomb lattice is cut, will also follow the boundary condition

$$C_h \cdot \kappa = 2\pi q \quad (4.5)$$

where is the cutting line along graphene and q is an integer number. Depending on where graphene energy bands are along the cutting line, the corresponding CNT will become metallic or a semiconductor. In Figure 1, the metallic and semiconducting CNTs are mapped out, and a pattern emerges with CNTs with their chiralities —m-n— being a multiple of 3 emerging as metals. Single CNTs exhibit polarization dependence with the electric field in optical selection rules, i.e. the possible transitions from one quantum state to another [14]. The polarization dependence is only strong in zigzag type nanotubes however. The dipole operator in anti chiral tubes will have a parity of -1 in the horizontal plane dipole operator along the z-axis and a +1 parity for dipole vectors along the x, y plane. For z polarized light there is no electronic band transition, while for light polarized perpendicular to the z axis, the angular momentum quantum number can shift by 1. Thus, CNTs will absorb light with the optical polarization parallel to the axial direction of the tube, but in a bundle or grouping of random-oriented CNTs, there will be no polarization dependence.

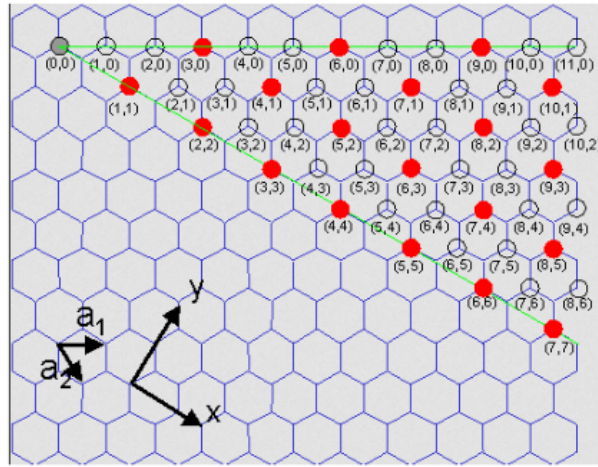


Figure 4.1: REPLACE Chiralities of CNTs with red dots indicating metallic and open dots [10].

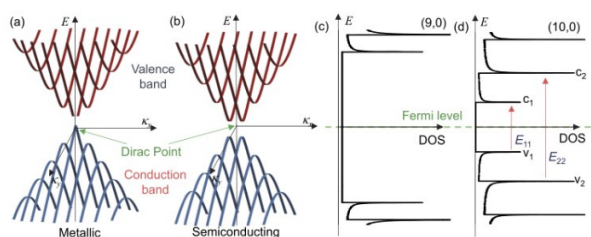


Figure 4.2: REPLACE Bands for (a)(c)Metallic and (b)(d)Semiconducting CNTs and their energy band gaps [12]

In the same year as the emergence of CNTs as a unique material, H. Kataura measured the optical absorption spectra of CNTs of various diameter CNTs performing photothermal deflection spectroscopy, which measures heat produced during relaxation of the electron hole pair generated by the absorbed light [15], an example of the optical absorption spectra are shown in Figure 4. While the absorption spectra across various CNT samples were consistent, the peak positions varied. Using the energy dispersion relations for pi-bands of the graphite [15]

$$E_{2D} = \pm \gamma \sqrt{1 + 4\cos(\frac{\sqrt{3}k_x a}{2})\cos(\frac{k_y}{2}) + 4\cos^2(\frac{k_y}{2})} \quad (4.6)$$

where  $\gamma$  is the overall integration and  $a$ ,  $k_x$ ,  $k_y$  are the reciprocal lattice vectors, fulfilling the periodic boundary condition for chiral vectors from Eq. (5), the one-dimensional energy band of CNTs could be calculated. Referring to Figure 3, the spikes in the DOS correspond to the energy levels of the optical transitions. Plotting the Gap energies from this model against the nanotube diameter in Figure 5, referred to commonly as a Kataura plot, shows how the first transition energy of CNTs has a relationship to the diameter by

$$E_{11} = \frac{2\gamma a_{C-C}}{d} \quad (4.7)$$

and the average band gap energies split along semiconductor and metallic chiral values. In short the absorption peak wavelength of a nanotube sample is determined by the mean tube diameter, and the absorption spectral bandwidth will be determined by the tube diameter distribution of the CNT sample.

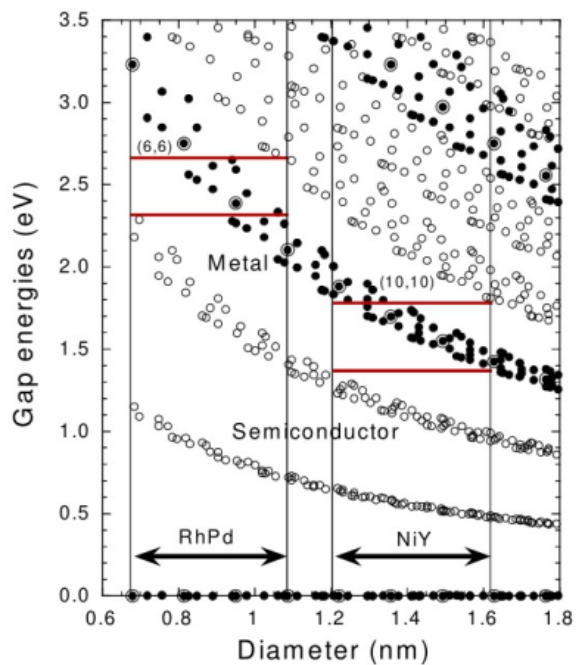


Figure 4.3: Chiralities of CNTs with red dots indicating metallic and open dots Calculated gap energies between mirror-image spikes in density of states for  $\gamma = 2.75$  eV. For (solid circles) metallic and (open circles) semiconducting, and (double circles) armchair CNTs. [15].

## 4.2 Nonlinear Optical Properties of CNTs

The general relationship between the polarization and electric field of a material is defined [16] as

$$P(t) = \epsilon_0(\chi^{(1)}E(t) + \chi^{(2)}E^2(t) + \chi^{(3)}E^3(t) + \dots) \quad (4.8)$$

where  $\epsilon_0$  is the linear susceptibility and  $\chi^{(2)}$  are the second and third order susceptibility. Due to the inversion symmetry of the CNT's structure, the second-order susceptibility is zero. However, a large third-order nonlinearity in CNTs has been measured [21] and is theorized to be a product of the one dimensional motion of the delocalized  $\pi$ -band electrons at a fixed lattice ion configuration [22]. The third-order nonlinearity is responsible for the saturable absorption of a material as well as the nonlinear Kerr effect. The refractive index as defined (4.9) is composed of the real part of the third-order susceptibility with  $I$  defining the optical intensity and  $\omega$  the optical angular frequency, and  $n$  is the nonlinear refractive index.

$$n = n_0 + n_2I = n_0 + \frac{3Re[\chi^{(3)}]}{4\epsilon_0 c n_0^2} I \quad (4.9)$$

The absorption coefficient defined by (4.10) is composed of the imaginary part of the third-order susceptibility and  $\alpha_0$ , and  $\alpha_{int}$  are the linear absorption coefficient, the non saturable absorption coefficient, and refractive index respectively.

$$\alpha = \frac{\alpha_0}{1 + \frac{I}{I_S}} + \alpha_{int} \sim \alpha_0 + \alpha_{int} + \frac{3\omega Im[\chi^{(3)}]}{2\epsilon_0 c^2 n_0^2} I \quad (4.10)$$

The saturation intensity,  $I_S$ , is the power per unit area it takes in a steady state to reduce the absorption to 1/2 the unbleached (or completely saturated) value and can be written in terms of

$$I_S = \frac{hf}{\sigma\tau} = \frac{E_S}{\tau} \quad (4.11)$$

where  $\sigma$  is the absorption cross section and  $E_S$  is the saturation fluence, which is the fluence (i.e. energy per unit area) it takes to reduce the initial fluence value to  $e^{-1}$  and  $\tau$  is the recovery time of the material.

The saturable absorption, as defined by (4.11), is a phenomenon where high intensity light will reduce the absorption of a material, but at weak intensity, the light will be absorbed and cause attenuation. This property of materials with strong third-order susceptibility like CNTs can be used to filter out weaker optical signals in noisy optical pulses, while simultaneously allowing strong pulses to pass through. Saturable absorption is observed in all materials with optical absorption resulting from electron transition

between two energy levels [14], but it is rare to find materials that have a recovery time that has a fast recovery time compared to the pulse duration, which in ultra-fast laser applications is in the few picosecond to femtosecond range. The ultra-fast response time of CNTs is only true however for bundles of CNTs with variations in their diameter due to entanglement between semiconducting and metallic via electrons tunneling and coupling from semiconducting CNTs to metallic CNTs [17].

### 4.3 Fluorescence of CNTs

The first Van Hove optical transition (E11) corresponds to the emission frequency and the second Van Hove optical transition (E22) corresponds to the excitation frequency. Equations for first and second van Hoven Transitions optical transition wavelengths as a function of diameter in nanometers and chiral angle are degrees derived in [19], but parameters from [18], which were found by fitting to data of samples of individual SWNT in aqueous sodium dodecyl sulfate (SDS) suspension and are valid for CNT diameters greater than 0.5nm. The parameters differ for each CNT “group”, i.e  $(n-m) \bmod 3 = 1$  is group 1  $(n-m) \bmod 3 = 2$  is group 2  $(n-m) \bmod 3 = 0$  are metallic CNTs and do not fluoresce.

Though it is unknown what specific effects contribute to the fitted parameters with the particular samples used, [18]found that other aqueous solutions have comparative spectral shifts of less than 2% compared to the equations when compared to other published results. Comparing to an experimental PL map using a different solutio[20], the equation results match quite well (the CNTs present in the left sample are marked in red on the right plot). We can see the expected variation from different solutions, for example CNT (10, 8) has a slightly higher excitation wavelength and slightly lower emission wavelength in SDS than in the NaDDBS/D<sub>2</sub>O solutions.

Only fully intact and individually dispersed semiconducting CNTs emit fluorescence CNTs coatings or placed on a substrate don't really fluoresce Interactions between CNTs typically cause quenching effects Though certain materials/solvents (varies with each CNT) can increase fluorescence Isolation is one of the largest factors in quantum yield Only in semiconductor-type CNTs

Desired type of CNTs can be targeted and isolated in a single step using modified aqueous two-phase extraction(ATPS). Hydration modulating agents are mixed in to tune the arrangement of surfactants on their surface

Depending on the mixture, selected CNTs turn highly hydrophobic or hydrophilic

Spectral shift due to the change in the local dielectric environment surrounding CNTs created by solvents and adsorbed molecules.[23]

$$(Emission)\lambda_{11} = \left[ \frac{1e7(cm^{-1})}{157.5 + 1066.9d_t} - 771(cm^{-1})\frac{\cos(3\theta)^{1.374}}{d_t^{2.272}} \right]^{-1} \quad (4.12)$$

$$(Excitation)\lambda_{22} = \left[ \frac{1e7(cm^{-1})}{145.6 + 575.7d_t} + 1326(cm^{-1})\frac{\cos(3\theta)^{0.828}}{d_t^{1.809}} \right]^{-1} \quad (4.13)$$

$$(Emission)\lambda_{11} = \left[ \frac{1e7(cm^{-1})}{157.5 + 1066.9d_t} + 347(cm^{-1})\frac{\cos(3\theta)^{0.886}}{d_t^{2.129}} \right]^{-1} \quad (4.14)$$

$$(Excitation)\lambda_{22} = \left[ \frac{1e7(cm^{-1})}{145.6 + 575.7d_t} - 1421(cm^{-1})\frac{\cos(3\theta)^{1.110}}{d_t^{2.497}} \right]^{-1} \quad (4.15)$$

Group 1 v. Group 2 Group 1 CNTs have lower Stokes shifts than Group 2 Group 1 have small chiral angles ( $\leq 20^\circ$ ) Group 2 span full  $0^\circ$  to  $30^\circ$  chiral angle range, but are grouped along chiral number difference ( $n - m$ )

Excitation/Emission wavelengths Increase in Stokes shifts with diameter along chiral difference ( $n - m$ ) lines Noted in red on lower plot, connected by black lines Increase in ex/em wavelengths with diameter

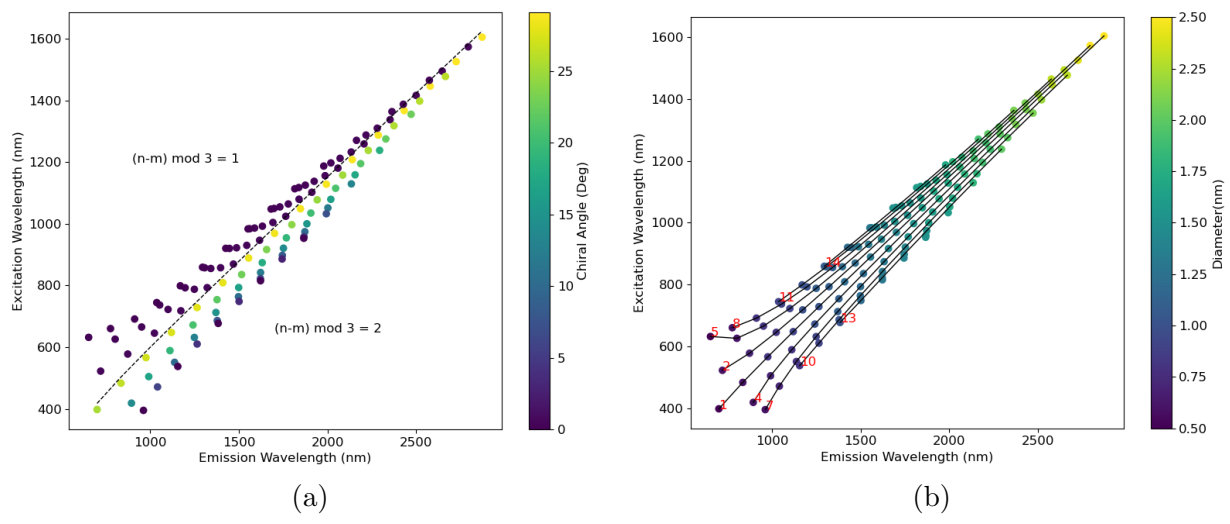


Figure 4.4: Group characteristics of CNTs colored by (a)chiral angle and (b)diameter

# Chapter 5

## Optical Excitation of Semiconductor Nanoparticles in Hollow-Core Fiber

### 5.1 Bandgap Overlap

Table shows all hollow-core fiber types available from ThorLabs and the central operating wavelengths for air-filled and D<sub>2</sub>O-filled fibers. The “air” range can be used for fibers that are selectively core-filled with D<sub>2</sub>O. The ranges for HC1550 and HC800B are approximated from spectrum measurements and HC2000 and HC1060 are taken from ThorLabs datasheets. The D<sub>2</sub>O central wavelengths are calculated using the band-gap shift equation

HCPCF	$\lambda_{AIR}$ (nm)	$\lambda_{D_2O}$ (nm)	Range (nm)
HC2000	2000	1144	250
HC1550	1550	887	500
HC1060	1060	606	100
HC800B	800	457	200

Table 5.1: Thorlabs fiber bandgap shift.

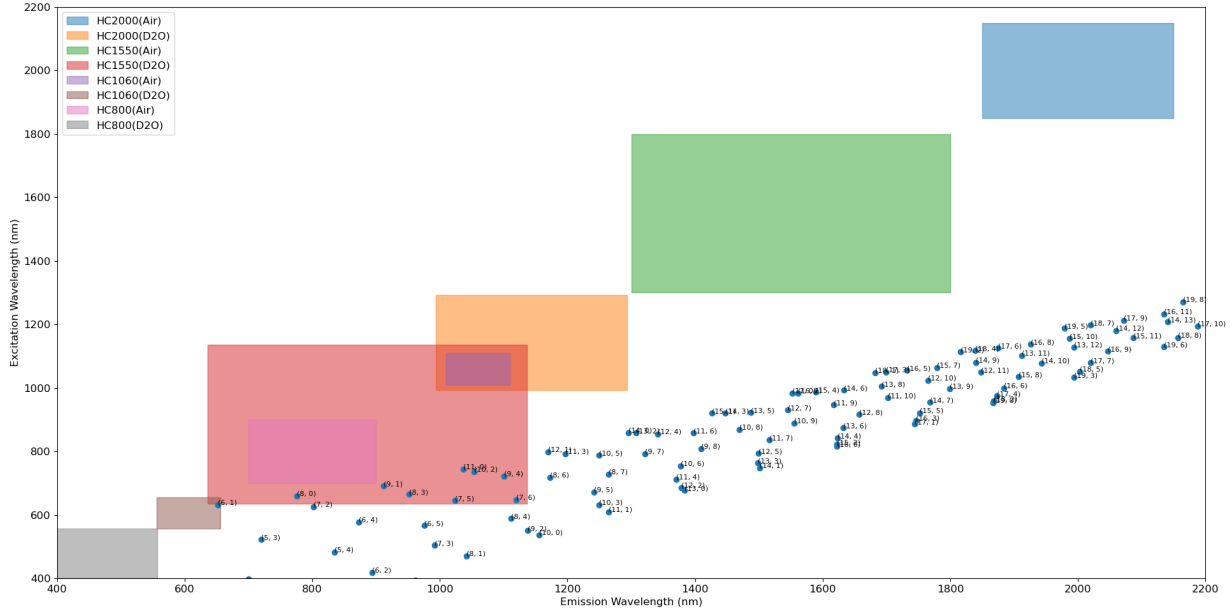


Figure 5.1: Hollow-core fiber bandgap overlayed on CNT emission vs. excitation wavelengths

$(n, m)$	$dt$ (nm)	$\Theta$ (deg)	$\lambda_{11}$ (nm)	$\lambda_{22}$ (nm)
(6, 1)	0.52	0.13	652.62	631.79
(7, 2)	0.65	0.21	802.05	625.92
(7, 5)	0.83	0.43	1023.74	645.33
(7, 6)	0.89	27.46	1119.76	647.64
(8, 0)	0.64	0	776.01	660.25
(8, 3)	0.78	0.27	951.61	665.39
(9, 1)	0.76	0.09	912.1	691.29
(9, 4)	0.92	0.31	1100.63	722.39
(10, 2)	0.88	0.16	1053.43	736.68
(11, 0)	0.87	0	1036.93	744.57

Table 5.2: CNTs with emission and excitation transmittable through HC1550 filled with D<sub>2</sub>O.

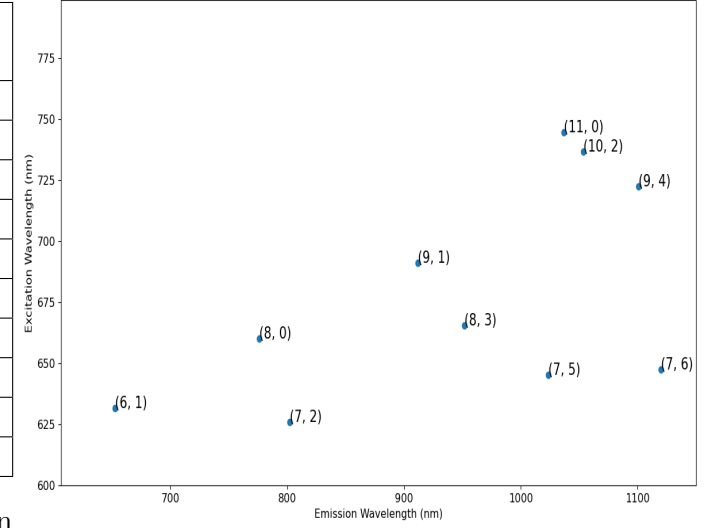


Figure 5.2: 1550HC CNTs

### 5.1.1 Experiment Set-Up

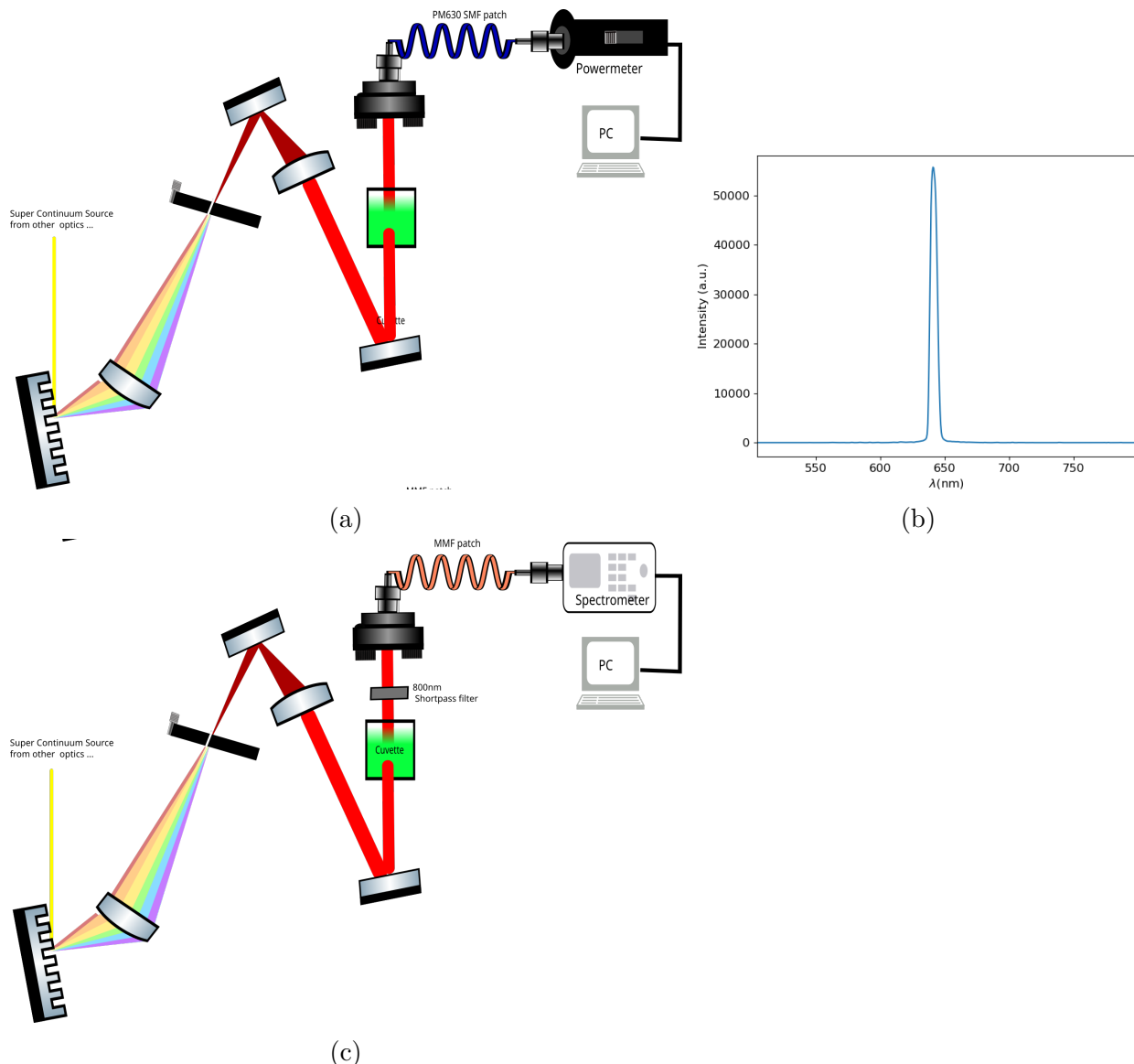


Figure 5.3: (a) (b)fwhm=6nm (c)

## Sample History

CNT samples were prepared by HeeBong Yang from the QuIN Lab at the University of Waterloo. SG65i powder was purchased from Sigma Aldrich and Dispersed in a surfactant at an initial powder concentration of  $1\text{mg}/1\text{mL}$ . The sample then underwent a procedure of purification steps, sorting with polymers & surfactants, and polymer exchange. The end condition of the sample was 65% (7,5), (7,6) dominant SWCNTs in DI water with 0.04% DOC, but at an unknown concentration.

## Sample Characteristics

CNT solutions follow Beer-Lambert's Law [40, 43],  $A = \log(\frac{I_{in}}{I_{out}}) = \varepsilon CL$  so the concentration can be deduced from the measured absorbance Fig.5.4(a) and the average previously reported extinction coefficient[41, 42, 43]  $\varepsilon = 30.98\text{mLmg}^{-1}\text{cm}^{-1}$  estimate a sample concentration around  $0.0042 \pm 0.0007(\text{mg/mL})$  Unfortunately no PL was detected from the

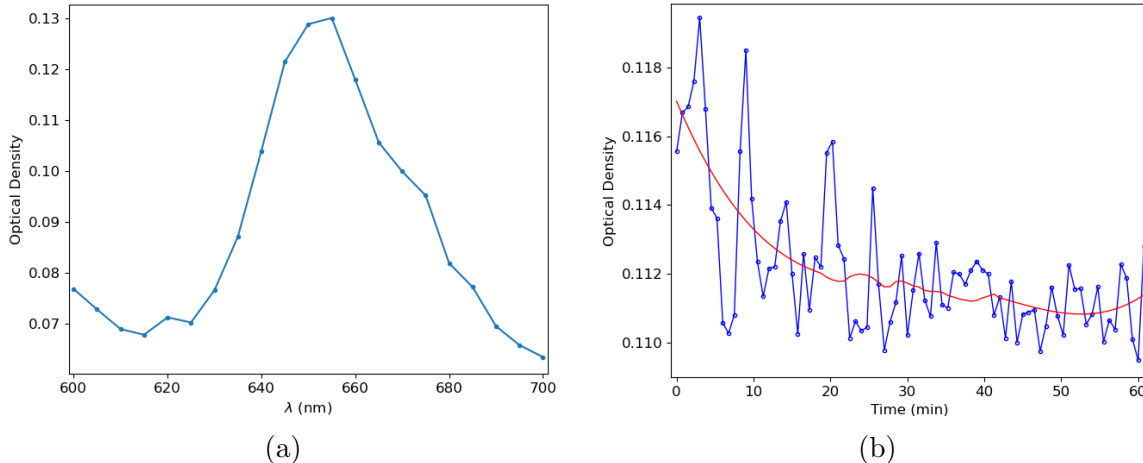


Figure 5.4: (a) Absorbance spectrum of CNT sorted CNT sample (b)Absorbance of CNT sorted sample over 60 minutes, very low photobleaching.

sample. There is 23.25% pm 10% decrease in PL intensity when using  $\text{H}_2\text{O}$  instead of  $\text{D}_2\text{O}$  for (7, 5) and 42.5% pm 5% for (7,6) %[39]. In combination with a  $48\mu\text{W}$  source when currently QY are expected to be around (7, 5)  $1.04 \pm 0.10\%$  , (7, 6)  $1.40 \pm 0.09$  could explain the lack of detection. Trying thinner cuvette, diluting the sample as self-quenching is also common, and preparation of a  $\text{D}_2\text{O}$  sample.

### 5.1.2 Expected Metrics

SWNT Fluorescence Action Cross Sections (7, 5) 3.2 ( $10^{-19}(cm^2/molC)$ (7, 6)2.3( $10^{-19}(cm^2/molC)$ ) [44] -optical density -expected efficiency

# Chapter 6

## Conclusion

This work studies variation in the refractive index contrast of HCPCFs and their use as a liquid-waveguide. We were able to demonstrate the preservation of light bandgap guidance through liquid by experimentally confirm the scaling laws for liquid-filled fibers of H<sub>2</sub>O and D<sub>2</sub>O. The main results of the thesis culminate in measuring the interaction of suspended ICG particles within the mode of the fiber, demonstrating the potential of creating fluorescent light sources out of suspended particles in liquid core fibers.

The unique optical properties of semiconducting CNTs are introduced and an argument for their suitability as a fluorescent light source is explored. For common commercially available HCPCF, 1550nm HCPCF is the most practical as it has the only bandgap that overlaps with the absorption and emission spectrum of several chiralities.

While the results of suspended ICG particles are promising and show a proof-of-concept, the progression to suspended CNTs in HCPCF is incomplete. The initial tests with a sorted CNTs sample were inconclusive and more time needs to be spent on producing a high-fluorescence sample. More work needs to be done experimentally with the CNTs and continuing efforts will hopefully lead to uses in fiber-integrated devices. Besides the CNT samples, one of the main challenges that remains is consistent and high coupling to the 1550nm HCPCF. Butt-coupled mechanical splicing chips fabricated for 800nm HCPCF consistently achieve coupling around 75-80% and robustly hold the fibers together[7], but the same recipe does not produce high-fidelity butt-coupled mechanical splicing chips for 1550nm HCPCF. This is another avenue that needs to be explored but is a very solvable problem.

### **6.0.1 Future Work**

what is ECDL fiber-integration diagram advantages.

# References

- [1] Yariv, Amnon and Pochi Albert Yeh, Optical Waves in Crystals: Propagation and Control of Laser Radiation," 1st ed. Wiley-Interscience, 2002.
- [2] J. D. Joannopoulos, Photonic crystals: molding the flow of light, 2nd ed. Princeton: Princeton University Press, 2008.
- [3] P. R. Villeneuve and M. Piché', "Photonic band gaps in two-dimensional square and hexagonal lattices," Phys. Rev. B, vol. 46, no. 8, pp. 4969–4972, Aug. 1992, doi: 10.1103/PhysRevB.46.4969.
- [4] I. A. Sukhoivanov and I. V. Guryev, Photonic Crystals: Physics and Practical Modeling, vol. 152. Berlin, Heidelberg: Springer Berlin Heidelberg, 2009. doi: 10.1007/978-3-642-02646-1.
- [5] T. A. Birks, D. M. Bird, T. D. Hedley, J. M. Pottage, and P. St. J. Russell, "Scaling laws and vector effects in bandgap-guiding fibres," Opt. Express, vol. 12, no. 1, p. 69, 2004, doi: 10.1364/OPEX.12.000069.
- [6] G. Antonopoulos, F. Benabid, T. A. Birks, D. M. Bird, J. C. Knight, and P. St. J. Russell, "Experimental demonstration of the frequency shift of bandgaps in photonic crystal fibers due to refractive index scaling," Opt. Express, vol. 14, no. 7, p. 3000, 2006, doi: 10.1364/OE.14.003000.
- [7] R. A. Maruf and M. Bajcsy, "On-chip splicer for coupling light between photonic crystal and solid-core fibers," Appl. Opt., vol. 56, no. 16, p. 4680, Jun. 2017.
- [8] L. Xiao, W. Jin, M. S. Demokan, H. L. Ho, Y. L. Hoo, and C. Zhao, "Fabrication of selective injection microstructured optical fibers with a conventional fusion splicer," Opt. Express, vol. 13, no. 22, p. 9014, 2005.

- [9] S. Kedenburg, M. Vieweg, T. Gissibl, and H. Giessen, “Linear refractive index and absorption measurements of nonlinear optical liquids in the visible and near-infrared spectral region,” *Opt. Mater. Express*, vol. 2, no. 11, p. 1588, Nov. 2011.
- [10] S. Dresselhaus, “PHYSICS OF CARBON NANOTUBES,” *Carbon*, 33(7), 883–891, 1995.
- [11] V. Popov, “Carbon nanotubes: properties and application,” *Materials Science and Engineering: R: Reports*, vol. 43, no. 3, pp. 61–102, Jan. 2004.
- [12] S. Yamashita, “Nonlinear optics in carbon nanotube, graphene, and related 2D materials,” *APL Photonics*, vol. 4, no. 3, p. 034301, Mar. 2019.
- [13] R. Saito, M. Fujita, G. Dresselhaus, and M. S. Dresselhaus, “Electronic structure of chiral graphene tubules,” *Appl. Phys. Lett.*, vol. 60, no. 18, pp. 2204–2206, May 1992.
- [14] C. Thomsen, S. Reich, and J. Maultzsch, *Carbon Nanotubes: Basic Concepts and Physical Properties*, 1st ed. Wiley, 2004.
- [15] H. Kataura et al., “Optical properties of single-wall carbon nanotubes,” *Synthetic Metals*, vol. 103, no. 1–3, pp. 2555–2558, Jun. 1999.
- [16] S. Yamashita, “A Tutorial on Nonlinear Photonic Applications of Carbon Nanotube and Graphene,” *J. Lightwave Technol.*, vol. 30, no. 4, pp. 427–447, Feb. 2012.
- [17] A. Gambetta et al., “Sub-100 fs two-color pump-probe spectroscopy of Single Wall Carbon Nanotubes with a 100 MHz Er-fiber laser system,” p. 8, 2008.
- [18] R. B. Weisman and S. M. Bachilo, “Dependence of Optical Transition Energies on Structure for Single-Walled Carbon Nanotubes in Aqueous Suspension: An Empirical Kataura Plot,” *Nano Lett.*, vol. 3, no. 9, pp. 1235–1238, Sep. 2003.
- [19] S. M. Bachilo, M. S. Strano, C. Kittrell, R. H. Hauge, R. E. Smalley, and R. B. Weisman, “Structure-Assigned Optical Spectra of Single-Walled Carbon Nanotubes,” *Science*, vol. 298, no. 5602, pp. 2361–2366, Dec. 2002.
- [20] S. Giordani et al., “Debundling of Single-Walled Nanotubes by Dilution: Observation of Large Populations of Individual Nanotubes in Amide Solvent Dispersions,” *J. Phys. Chem. B*, vol. 110, no. 32, pp. 15708–15718, Aug. 2006.

- [21] A. Martinez and S. Yamashita, "Carbon Nanotube-Based Photonic Devices: Applications in Nonlinear Optics," In: J. M. Marulanda, Ed., Carbon Nanotubes Applications on Electron Devices, InTech, 2011.
- [22] Vl. A. Margulis and T. A. Sizikova, "Theoretical study of third-order nonlinear optical response of semiconductor carbon nanotubes," *Physica B: Condensed Matter*, vol. 245, no. 2, pp. 173–189, Mar. 1998.
- [23] E. Turek, T. Shiraki, T. Shiraishi, T. Shiga, T. Fujigaya, and D. Janas, "Single-step isolation of carbon nanotubes with narrow-band light emission characteristics," *Sci Rep*, vol. 9, no. 1, p. 535, Dec. 2019
- [24] M. Bajcsy et al., "Laser-cooled atoms inside a hollow-core photonic-crystal fiber," *Phys. Rev. A*, vol. 83, no. 6, p. 063830, Jun. 2011, doi: 10.1103/PhysRevA.83.063830.
- [25] A. P. Hilton, C. Perrella, F. Benabid, B. M. Sparkes, A. N. Luiten, and P. S. Light, "High-efficiency cold-atom transport into a waveguide trap," *Phys. Rev. Applied*, vol. 10, no. 4, p. 044034, Oct. 2018, doi: 10.1103/PhysRevApplied.10.044034. A
- [26] P. Domokos, P. Horak, and H. Ritsch, "Quantum description of light-pulse scattering on a single atom in waveguides," *Phys. Rev. A*, vol. 65, no. 3, p. 033832, Mar. 2002, doi: 10.1103/PhysRevA.65.033832.
- [27] M. T. Manzoni, "New Systems for Quantum Nonlinear Optics," . 2017, Thesis, p. 39-40.
- [28] X. Fang et al., "One-step condensation synthesis and characterizations of indocyanine green," *Results in Chemistry*, vol. 3, p. 100092, Jan. 2021, doi: 10.1016/j.rechem.2020.100092.
- [29] W. Holzer et al., "Photostability and thermal stability of indocyanine green," *Journal of Photochemistry and Photobiology B: Biology*, vol. 47, no. 2-3, pp. 155-164, Dec. 1998.
- [30] M. L. Landsman, G. Kwant, G. A. Mook, and W. G. Zijlstra, "Light-absorbing properties, stability, and spectral stabilization of indocyanine green," *Journal of Applied Physiology*, vol. 40, no. 4, pp. 575–583, Apr. 1976.
- [31] M. Mauerer, A. Penzkofer, and J. Zweck, "Dimerization, J-aggregation and J-disaggregation dynamics of indocyanine green in heavy water," *Journal of Photochemistry and Photobiology B: Biology*, vol. 47, no. 1, pp. 68–73, Nov. 1998.

- [32] F. Rotermund, R. Weigand, W. Holzer, M. Wittmann, and A. Penzkofer, “Fluorescence spectroscopic analysis of indocyanine green J aggregates in water,” *Journal of Photochemistry and Photobiology A: Chemistry*, vol. 110, no. 1, pp. 75–78, Oct. 1997.
- [33] R. Philip, A. Penzkofer, W. Bäumler, R. M. Szeimies, and C. Abels, “Absorption and fluorescence spectroscopic investigation of indocyanine green,” *Journal of Photochemistry and Photobiology A: Chemistry*, vol. 96, no. 1–3, pp. 137–148, May 1996.
- [34] V. Saxena, M. Sadoqi, and J. Shao, “Degradation Kinetics of Indocyanine Green in Aqueous Solution,” *Journal of Pharmaceutical Sciences*, vol. 92, no. 10, pp. 2090–2097, Oct. 2003.
- [35] D. Farrakhova et al., “Fluorescence imaging analysis of distribution of indocyanine green in molecular and nanoform in tumor model,” *Photodiagnosis and Photodynamic Therapy*, vol. 37, p. 102636, Mar. 2022, doi: 10.1016/j.pdpdt.2021.102636.
- [36] E. Spartalis et al., “Intraoperative Indocyanine Green (ICG) Angiography for the Identification of the Parathyroid Glands: Current Evidence and Future Perspectives,” *In Vivo*, vol. 34, no. 1, pp. 23–32, 2020, doi: 10.21873/invivo.11741.
- [37] D. J. DeDora et al., “Sulfobutyl ether  $\beta$ -cyclodextrin and methyl  $\beta$ -cyclodextrin enhance and stabilize fluorescence of aqueous indocyanine green: Sulfobutyl Ether  $\beta$ -Cyclodextrin and METHYL  $\beta$ -Cyclodextrin,” *J. Biomed. Mater. Res.*, vol. 104, no. 7, pp. 1457–1464, Oct. 2016, doi: 10.1002/jbm.b.33496.
- [38] R. Weigand, F. Rotermund, and A. Penzkofer, “Degree of aggregation of indocyanine green in aqueous solutions determined by Mie scattering,” *Chemical Physics*, vol. 220, no. 3, pp. 373–384, Aug. 1997, doi: 10.1016/S0301-0104(97)00150-X.
- [39] X. Wei et al., “Photoluminescence Quantum Yield of Single-Wall Carbon Nanotubes Corrected for the Photon Reabsorption Effect,” p. 23.
- [40] F. Schöppler et al., “Molar Extinction Coefficient of Single-Wall Carbon Nanotubes,” *J. Phys. Chem. C*, vol. 115, no. 30, pp. 14682–14686, Aug. 2011, doi: 10.1021/jp205289h.
- [41] A. J. Blanch, C. E. Lenehan, and J. S. Quinton, “Parametric analysis of sonication and centrifugation variables for dispersion of single walled carbon nanotubes in aqueous solutions of sodium dodecylbenzene sulfonate,” *Carbon*, vol. 49, no. 15, pp. 5213–5228, Dec. 2011, doi: 10.1016/j.carbon.2011.07.039.

- [42] A. Ansón-Casaos, J. M. González-Domínguez, I. Lafragüeta, J. A. Carrodeguas, and M. T. Martínez, “Optical absorption response of chemically modified single-walled carbon nanotubes upon ultracentrifugation in various dispersants,” *Carbon*, vol. 66, pp. 105–118, Jan. 2014, doi: 10.1016/j.carbon.2013.08.048.
- [43] S. H. Jeong, K. K. Kim, S. J. Jeong, K. H. An, S. H. Lee, and Y. H. Lee, “Optical absorption spectroscopy for determining carbon nanotube concentration in solution,” *Synthetic Metals*, vol. 157, no. 13–15, pp. 570–574, Jul. 2007, doi: 10.1016/j.synthmet.2007.06.012.
- [44] D. A. Tsyboulski, J.-D. R. Rocha, S. M. Bachilo, L. Cognet, and R. B. Weisman, “Structure-Dependent Fluorescence Efficiencies of Individual Single-Walled Carbon Nanotubes,” *Nano Lett.*, vol. 7, no. 10, pp. 3080–3085, Oct. 2007, doi: 10.1021/nl071561s.